

Politecnico Di Torino

College of Electrical Engineering, Telecommunications and Physics (ETF)

Master of Science in NANOTECHNOLOGIES FOR ICTs



Impact of sputtering process conditions on molybdenum oxides properties for silicon heterojunction solar cells

A master thesis submitted as partial fulfillment for the degree of Master of Science degree in Nanotechnologies
For ICTs

Student Name: Mohammed I. Elsmami

Promoter Name: Professor. Elena Tresso

Company Supervisor: Jinyoun Cho

Dec.2018

Dedication

This thesis work is dedicated to my wife and my kids who are patient waiting for me and my parents and my sister for their kindness and devotion, and for their endless support. To anyone in Polito, IMEC and KU-Leuven offered me his/her support.

Acknowledgement

First and foremost, I thank Professor. Tresso for the utmost support for this thesis to reach this step. I am forever indebted to Jinyoun Cho for his unwavering support, encouragements and patience through this process. I can never pay you back for all the help you have provided me, the experience you have helped me gain by working at IMEC/KU-Leuven and the precious time he spent making sure my thesis is always on track. Thank you so much! I am very fortunate and grateful to Dr.Maria for providing readership and ideas; paramount to the realization of this thesis. Thank you for your support and helpful suggestions, I will be forever thankful to you. To Professor Jef, I don't know where I would be now if it wasn't for your huge help in editing my many mistakes. You are truly an outstanding person and an able educator and, I thank you from the bottom of my heart. Not least of all, I owe so much to my whole family of Polito for their undying support, their unwavering belief that I can achieve so much. Unfortunately, I cannot thank everyone by name because it would take a lifetime but, I just want you all to know that you count so much. Had it not been for all your prayers and benedictions; were it not for your sincere love and help, I would never have completed this thesis. So thank you all.

Notice

This final thesis is based on internal, confidential data and information's of the following
enterprise: **IMEC/KU-Leuven**

This work may only be available to the first and second reviewers and authorized members
of the board of examiners. Any publication and duplication of this final thesis - even in part -
is prohibited. An inspection of this work by third parties requires the expressed admission
of the indicated above company

Abstract

Molybdenum Oxide has recently demonstrated -when deposited as a thin film- to be a promising passivating contact for solar cells offering favorable condition for hole collection from c-Si substrate, inducing upward band bending and reducing parasitic light absorption. Hole carrier selectivity represents a new development trend in research line for photovoltaic efficiency improvement. In particular, the main objective of this research work is optimization of RF-Sputtered MoO_x as hole selective contact for silicon heterojunction (SHJ) solar cells. Sputtering process is appealing because of its industrial relevance throughput and it has proven to be useful to tune the properties of metal oxides by varying the deposition conditions. First three chapters of this thesis mainly focus on the theoretical potentiality of adopting MoO_x hole selective contact in the emitter as replacement of conventional p-doped amorphous silicon layer. In SHJ solar cells the high parasitic light absorption of p-doped amorphous silicon layer can be reduced utilizing undoped transition metal oxides. MoO_x has in fact an optimal optical transmittance window response due to high band gap $\sim 3\text{eV}$ and ideally high work function $\sim 6.7\text{ eV}$. These facts allow for higher band bending characteristic and, as a consequence, hole carrier selectivity. For this reason, we employed thin layer of MoO_x obtained by RF- sputtering process followed by post-annealing process. While the first process has been optimized to yield desirable sub-stoichiometric MoO_x with low power deposition conditions (100W), high oxygen flow rate (100sccm) and mid-range value for Argon gas flow rate (100sccm), the annealing process time has been increased to obtain better cell performance in comparison with MoO_x deposited with thermal evaporation technique. Experimental results obtained on the wafer cell scale, such as pseudo cell efficiency of 14.9%, an acceptable open circuit voltage 465mV and flat band voltage of around 457mV. Moreover, XPS results revealed as-deposited effective work function around 6.08eV and reduced to 4.99eV after annealing. Layer structural analysis was performed with Transmission Electron Microscopy to investigate interfacial mixed layers and their probable impact on the final cell efficiency. A further detailed discussion on the possible Voc lowering factors is elaborated in the last section of chapter four. Final chapter, summed up the results and portrayed future promising outlook, showing that definitely more detailed research work on sputtered MoO_x on the factors may dominantly impact open circuit voltage such as interfacial layers investigation, work function optimization, and hence, solar cell efficiency improvement is required.

Table of Contents

List of Tables	8
List of Figures	9
I.Chpater One: Introduction	12
1.1 Importance of solar energy	12
1.2 Solar cell basic structure and physics	14
2.Chpater Two: Background And Literature Review.....	17
2.1 Passivated Emitter And Rear Contacts (PERC)	17
2.2 Silicon Heterojunction (SHJ).....	18
2.2.1 Optical losses in the passivation layers—impact on Short Circuit Current....	19
2.2.2 Charge collection losses in the absorption layers— impact on Open Circuit Voltage and Filing Factor	19
2.3 Transition Metal Oxide [TMO] for SHJ.....	20
2.3.1 TMOs Work Function	21
2.3.2 Hole Selective Contacts	22
2.4 Electronic Transport Mechanism in TMO.....	24
2.5 Molybdenum Oxide (MoO_x) as Hole Selective Contact.....	26
2.5.1 MoO_x -n-c-Si band diagram.....	26
2.5.2 MoO_x Oxidation States and High work function origin.....	27
2.6 Reported results of solar cell with MoO_x contacts.....	28
2.6.1 Annealing Impact on MoO_x contacted Solar Cell.....	29
2.7 Sputtering Process.....	30
2.8 Sputtered MoO_x For Solar Cells.....	31
3.Chapter Three: Experiments setup and Characterization Tools.....	34
3.1 Pre-deposition wafer cleaning	34
3.1.1 Contamination sources and Prevention Method.....	34
3.2 Deposition Process: RF-Sputtering Tool Parameters.....	35
3.3 Post-deposition annealing Process:.....	36

3.4 Sample Characterization and Measurements	36
3.4.1 Film Analysis.....	37
3.4.1.1 Film Thickness.....	37
3.4.1.2 XPS Analysis.....	37
3.4.1.3 ERDA Analysis.....	40
3.4.2 Electrical analysis	41
3.4.2.1 Photo-luminescent (PL) measurement.....	41
3.4.2.2 Open Circuit Voltage Measurement (SunsVoc)	44
3.4.2.3 Capacitance-Voltage Measurements.....	46
3.4.3 Structural analysis.....	47
3.4.3.1 TEM Characterization.....	47
4. Chapter Four: Results and Discussion.....	50
4.1 Deposition conditions study.....	50
4.1.1 Plasma power study.....	50
4.2 ERDA Detailed Analysis	54
4.3 XPS Measurement:.....	56
4.4 Passivation study.....	59
4.5 Band bending study C-V Measurement	60
4.6 TEM Characterization.....	62
4.7 Qualitative Loss analysis for low performance of sputtered MoO ₃	65
5. Chapter Five Conclusion and Future Outlook.....	71
5.1 Conclusion.....	71
5.2 Future Outlook.....	71
IV. References and Bibliography.....	74

List of Tables

Table.1	23
Table.2	35
Table.3	57
Table.4	60
Table.5	60

List of Figures

Fig.1	12
Fig.2	13
Fig.3	15
Fig.4	17
Fig.5	18
Fig.6	20
Fig.7	21
Fig.8	23
Fig.9	24
Fig.10	25
Fig.11	26
Fig.12	27
Fig.13	28
Fig.14	29
Fig.15	30
Fig.16	31
Fig.17	32
Fig.18	34
Fig.19	36
Fig.20	37
Fig.21	38
Fig.22.....	38
Fig.23.....	39
Fig.24	40
Fig.25	41
Fig.26	42
Fig.27	43
Fig.28	44
Fig.29	45

Fig.30	46
Fig.31	47
Fig.32	48
Fig.33	51
Fig.34	53
Fig.35	54
Fig.36	55
Fig.37	56
Fig.38	56
Fig.39	58
Fig.40	59
Fig.41	60
Fig.42	61
Fig.43	62
Fig.44	63
Fig.45	64
Fig.46	65
Fig.47	66
Fig.48	67

I. Chapter One: Introduction

I. Chapter One: Introduction

I.1 Importance of solar energy

The whole world seeks out the salvage from the conventional energy sources as they contribute significantly in carbon dioxide pollution. Moreover, conventional resources are prone to be depleted in the long run time. Gradually, according to Paris climate agreement and other general relevant trends, the contribution from clean, more efficient and cost-effective sources shall prevail [1]. Selection criteria amongst a variety of alternative sources is availability, technical feasibility and eco-socially feasible factors. To this end, photovoltaic-potentially- may fulfill this selection criterion. As a result, economical metrics of solar cells correlate between cell conversion efficiency and levelized cost of electricity (LCOE) (see Fig. 1 and Fig. 2). In this sense, there is proven inverse proportionality between them [2]. Technologically, solar cell suffers from low efficiency a raised from well-known and empirically proven theories (i.e. thermodynamic and Shockley-Queisser limits). To a great extent the former is tackled through well-known spectrum light trapping techniques, while the latter is mainly manifested in the internal quantum efficiency factor. Interestingly, light trapping techniques is another research line of interest with exploiting phenomenal nanostructure physical capabilities which is in terms of efficiency has already away promising research field. However, internal quantum efficiency is strongly function of carrier generation-recombination mechanism still to research to a bridge the gap in cell efficiency.

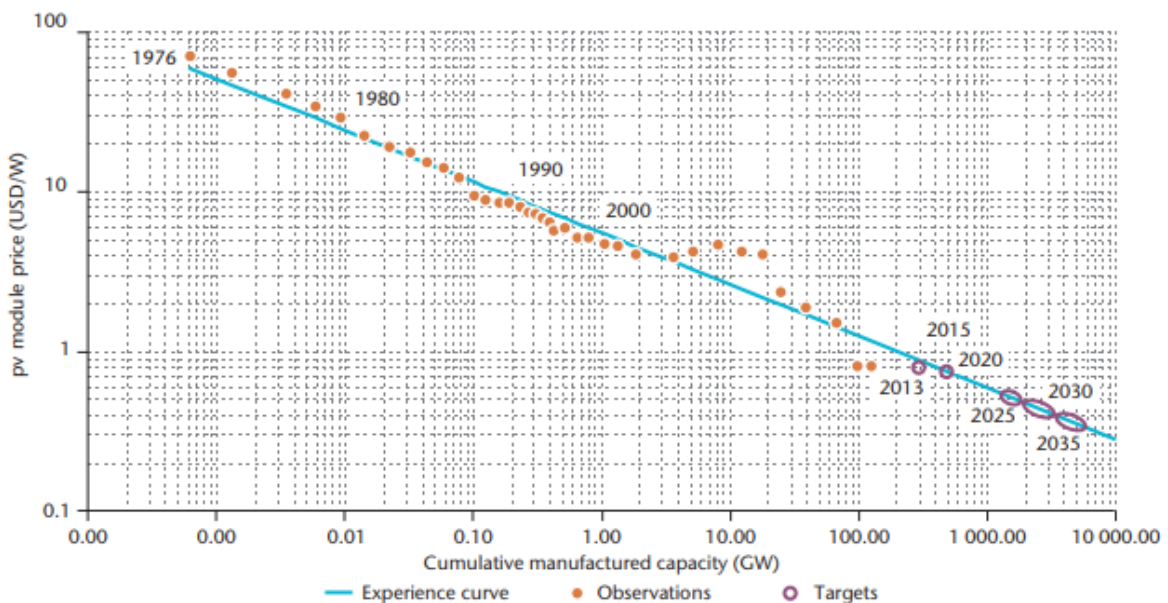


Fig.1 Past modules prices and projection to 2035 based on learning curve-from Ref. [2]

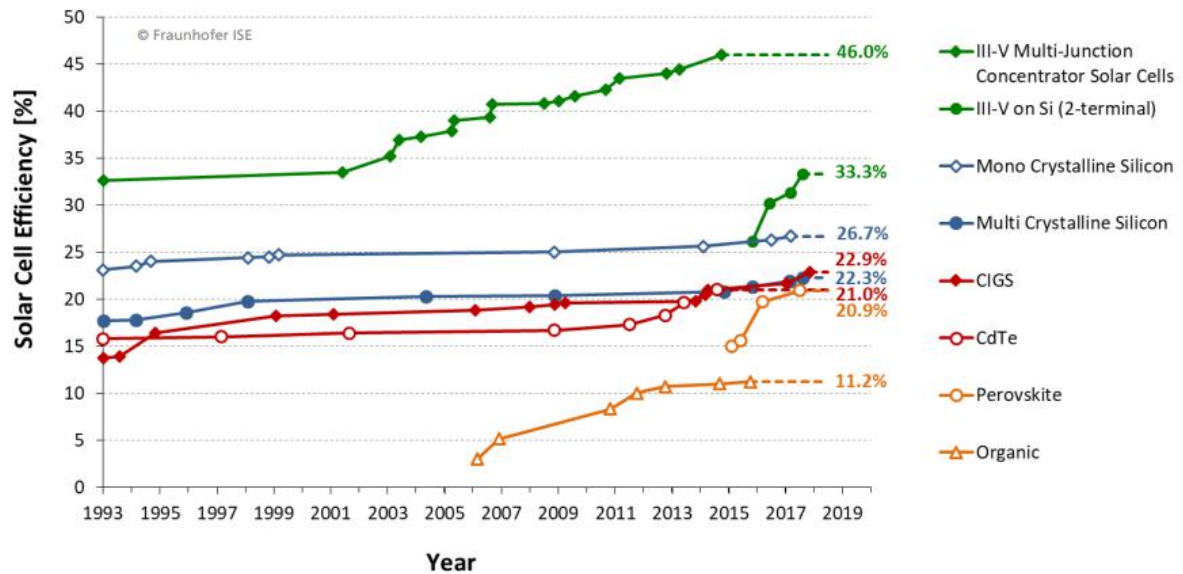


Fig.2 Solar cell efficiency trend until 2019 for various solar cell types by Fraunhofer ISE [2].

Concerning solar cell research optimization process, more carrier selectivity and heterostructure based solar cell grabs the lead over the conventional homojunction solar cell. Thanks to silicon heterojunction (SHJ) structure as it paved the way toward more interesting materials and various technological process. In “standard” SHJ design, electrons and holes collection are realized at opposite sides of the c-Si wafer. In this manner, device fabrication only relies on a few well-established processing steps without requiring patterning as in Industrial solar cells case, i.e. passivated emitter and rear contacts (PERC), rather, electron and hole collection is achieved by layer of n- and p-type amorphous silicon films [3]. Markedly, this structure has- industrially and academically – attracted attention because of the interesting electrical and optical properties it may render [3]. Further improvement revealed with replacement of doped n-type and p-type amorphous silicon layer due to parasitic absorption of light with Transition Metal Oxide (TMO). TMOs are interesting wide range of promising materials with low work function and high work function-based elements for electrons and holes respectively. Hence, TMO’s biggest advantages are concurrently low parasitic response of light and improved carrier selectivity [4].

In this work, one of hole selective contact family of TMOs is investigated , near stoichiometric Molybdenum Oxide (MoO_x) based structure is believed to be good candidate for hole contact selectivity for it’s wide bandgap and high work function which in turn allows for higher band bending for selective hole carrier transport [4]. By using high industrial throughput physical

deposition technique; radio frequency (RF) sputtering technique which is utilized to deposit MoO_x on passivated amorphous silicon (a-Si:H) and Crystallized silicon (c-Si) (i.e. hereinafter referred as Reference Structure), the objective of this research is to investigate the sputtering conditions that give rise to new solar cell typical structure with high hole carrier selectivity through using standard characterization measurements. Moreover, post-annealing process controlling parameters is also investigated.

In order to acquaint interested reader (s) with this topic, thesis is divided into five chapters following logical organization order. Beginning with Chapter one: Introduction of solar cell where a glimpse of basic solar cell structure and physics is presented, chapter two: background and literature review concerns the most important solar cells technologies which has given rise to the main thesis topic which investigated sputtered MoO_x structure. We tried in chapter two to present sections in logical manner with the most important silicon solar cell of interest along with schematic and electronic structure explanation (PERC, SHJ, SHJ with TMOs, Hole selective contact and MoO_x as the main topic of thesis for silicon Heterojunction solar cell). Where Chapter three: is more about experiment setup and characterization measurement theoretical overview, chapter four cares more about experimental results and discussion about the hole-contact with sputtered MoO_x . A qualitative loss analysis is presented to show probable reasons behind low yielded results of sputtered MoO_x on reference structure. Lastly, chapter five summarized the entire research chapters with brief conclusion and outlooks portraying open issues to be researched further by solar cell research community.

1.2 Solar cell basic structure and basic physics

Photovoltaics or solar cells are one of the most promising renewable energy source types. Nevertheless, solar cell generation era, solar cell is photo-electrical conversion device which converts the energy of light directly into electricity by the photovoltaic effect. The physical basis is photoelectrical generation effect and collection of generated electrons-holes pairs [4]. Hence, separated electrons and holes to be collected in the negative terminal and holes to the positive terminal respectively- thus generating electrical power. Basic solar cell structure is illustrated in Fig.3.

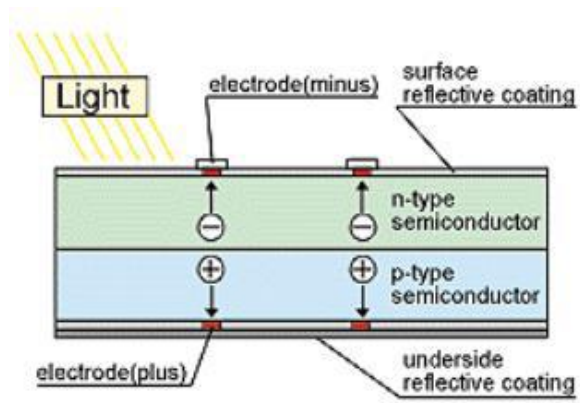


Fig.3 Basic solar cell structure where eletron-hole pairs are splitted and collected at contacts- from Ref.[5]

2. Chapter Two: **Background and** **Literature Review**

2. Chapter Two: Background and Literature Review

Following reviewing the well-known basic structure and physics of solar cells in chapter 'one', we are showing in sub-chapters (2.1, 2.2, 2.3 and 2.4), the logical evolution of MoO_x as hole selective contact layer for SHJ by revising in the logical order PERC, SHJ, TMOs and TMOs as hole selective contact basic structure and physics.

2.1 Passivated Emitter And Rear Contacts (PERC)

Silicon solar cells with passivated emitter and rear contacts (PERC) also known as backside passivation cell [6]. Industrial PERC cells using have demonstrated the average efficiency of 20.5% [6]. In a conventional solar cell, there is an aluminum metallization layer which makes contact across the full area of the back of the cell. The key features of PERC cells are: coating of the backside of the cell with a special dielectric layer that has tiny holes made by a laser [6]. Aluminum metallization is then applied on top of the dielectric layer (see Fig. 1. (a) and (b)) [6]. Basic advantages of PERC is the backside reflection of photons and blue light response on the front emitter contact side [6] (see Fig 1 (c) and (d)).

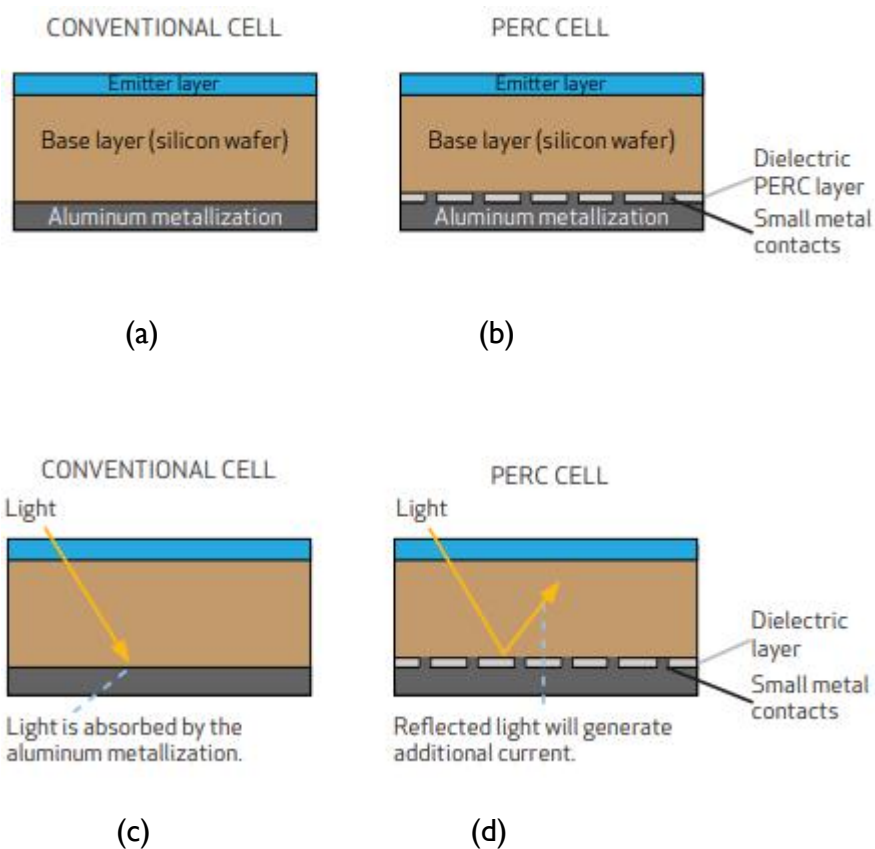


Fig. 4 (a) Cross-sectional structure of conventional solar cell and (b) Schematic of PERC solar cell (c) shows light absorption by backside contact in a conventional cell. (d) back side contact absorption is extremely prevented in PERC- from Ref. [7]

2.2 Silicon Heterojunction (SHJ)

Technological process complexity in previous industrial solar cell (PERC) has been improved in silicon heterojunction (SHJ) [3]. For instance, structuring and alignment steps as e.g. in partial rear contact (PRC) cells are not needed during cell production and geometrical constraints which caused by the need to optimize regions for either low recombination or efficient carrier extraction / transport [3]. Another anticipated improvement is cost reduction because of fabrication process simplicity. The thin absorber material of silicon Heterojunction (SHJ) solar cells are a promising high-efficiency cell design for which the higher production and material cost could be translate into lower costs per Watt peak (€/Wp) on module level [3]. The unique feature of SHJ cells is that, hole and electron selective contacts in the front and back side of the solar cell can be formed without significantly increasing the overall minority carrier recombination of the solar cell. SHJ is distinguished with two basic advantages of SHJ cells over the classical homojunction cells, first upside is that, the low minority carrier recombination with noticeable carrier selectivity allows for very high voltages at both open-circuit and maximum power point conditions. Second advantage over PERC is the absence of recombination at the metal/semiconductor contacts which is the most important feature that enables such low recombination losses [3]. This can clearly observed in the Fig.5 where electronic structure shows enhanced selectivity for electron and hole carrier at the contact [3].

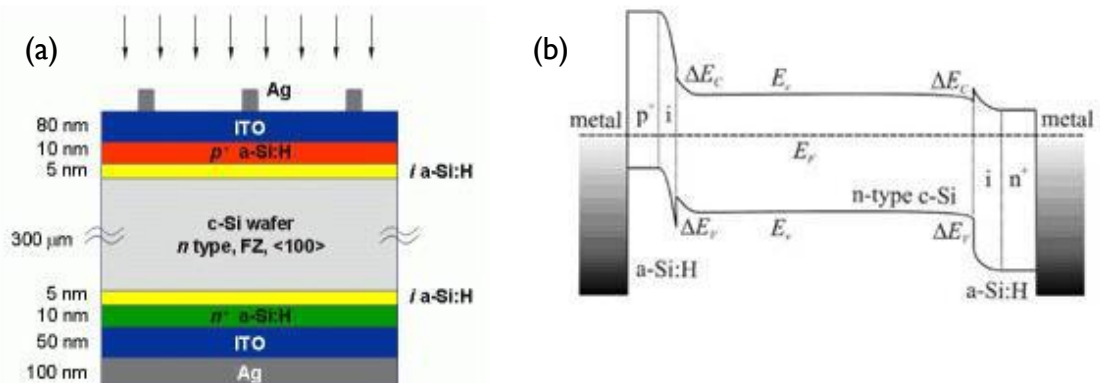


Fig.5 (a) Schematic diagram of typical heterojunction solar cell (b) Electronic band diagram in dark at equilibrium conditions of a heterojunction solar cell by EFPL[8]

2.2.1 Optical losses in the passivation layers—impact on Short Circuit Current

Main striking breakthrough in heterojunction solar cells is enhanced contact selectivity, however, one of the principal challenges is to find a wide-band-gap carrier-collecting contact at the front side to minimize parasitic absorption [9]. Although a-Si:H still having a relatively wider bandgap (1.7-1.8) eV than the c-Si absorber underneath, high doping of thin passivation layer of a-Si:H can lead to significant parasitic absorption and then give rise to reduced short circuit current J_{SC} in the cells. See Fig. 6 for comparable bandgap of passivating layer and cell-substrate [9].

2.2.2 Charge collection losses in the absorption layers— impact on Open Circuit Voltage and Filing Factor

The second challenge in SHJ solar cell contact is that, typical SHJ contact possess loss manifested in radiative and nonradiative recombination processes with high doping and interfacial defect, which in turn significantly reduce open circuit voltage (V_{OC}) if it is not carefully engineered well. Photo-generated carriers must be collected at the appropriate contacts to contribute to the Photo-Current (J_{pho}) [9]. Hence, Raghu et al. [9] summarized collection loss mechanisms for design and process optimization in Fig. 6, there are 5 process-specific parameters that dictate carrier loss in SHJ cells: 1) the thickness of the intrinsic a-Si:H layer (t_i), 2) p-layer doping (N_A), 3) intrinsic a-Si:H/n-doped c-Si valence band discontinuity (ΔE_V), 4) interface defect density (N_{IT}^F) and 5) absorber doping (N_D). The corresponding collection losses can be divided up into two groups; first one is recombination losses related to N_{IT} , which impact V_{OC} and second ones are heterojunction losses [influenced by ΔE_V , t_i , Band Bending [ϕ_p , and ϕ_N]], which impact the fill factor (FF) [9].

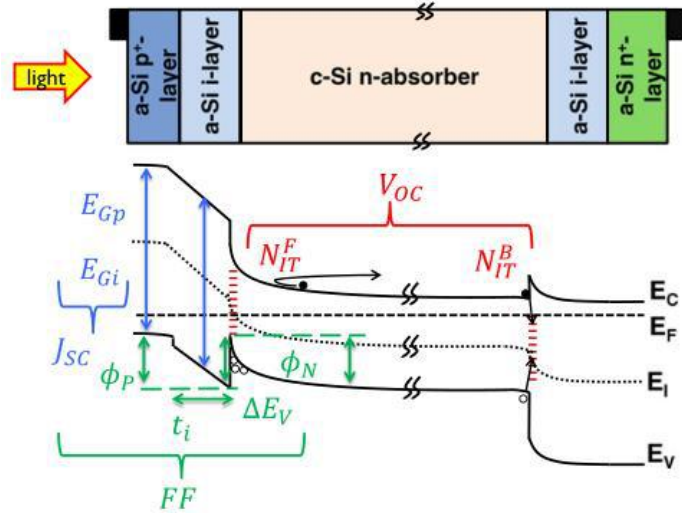


Fig. 6 An equilibrium energy band diagram illustrating the device parameters necessary for precisely evaluating the performance of SHJ cells. E_{Gp} , E_{Gi} are bandgaps of p- and i- a-Si:H layers, ϕ_P and ϕ_N are the band-bending in the front a-Si:H layer and the absorber regions of the junction, ΔE_V is valence band offset at a-Si/c-Si interface, t_i is i-layer thickness, N_{IT}^F and N_{IT}^B are interface defect densities at front and back a-Si/c-Si interfaces by Ref. [9].

2.3 Transition Metal Oxide (TMO) for SHJ

Transition Metal Oxide (TMO)s are possible contender where technological process lower complexity, excellent optical properties and improvement in the tradeoff between enhanced V_{oc} and low FF caused by ohmic losses which are induced by lateral electrical transport are the main improvement over SHJ cell [4] [10]. The TMOs are considered as semi-permeable charge transport layers substitute emitter layer in a SHJ silicon solar cell, however, in the recent novel structure, TMO layers are used as a part of contact layers for so called doping free SHJ solar cells. Hence, photovoltaic energy has potential to compete in terms of price with conventional energy sources. Cost reduction of TMO may reduce the prices of solar cells thanks to transition metal cheapness, abundance and provision of new low-cost deposition methods [4]. In contrast, TMOs exhibit poor electronic properties such as short carrier lifetime and low mobility of the excited charge carriers [4]

Adding two semi-permeable charge transport layers at both sides of the cell promote holes to be collected in one contact and electrons to be collected in the other one without having to create a standard p-n junction by doping processes. This enable the fabrication of solar cell devices without expensive processes involving toxic gases which are involved in typical doping process. TMOs catorgized into electron selective transport layer such as Titanium Oxide

(TiO₂) and Zinc Oxide (ZnO) and hole-transport such as layers Vanadium Penta-oxide (V₂O₅), Tungsten Trioxide (WO₃) and Molybdenum Trioxide (MoO₃) [4].

Physically, electronic band structure improvement stems up from band bending at interface layer. By adopting theoretical Anderson’s rule for band alignment in heterostructures, band offset can be evaluated. However, where the first dependance of (band offset) between two materials is also influenced by the properties of their interface, work function (WF) also depend somewhat on the exact composition and structure of each material, which in turn depend on the preparation method. Therefore, theoretical vacuum-referenced values Fig. 7 only give a rough indication of the band alignment. [10].

2.3.1 TMOs Work Function:

Obviously from Fig.7, potentially low work function materials serve as an electron-selective and high work function materials acts as a hole-selective contact for n doped absorber, respectively. However, this does not mean that carrier selectivity depends solely on band alignment, rather the work function of the material can also induce selectivity. The work function values for the transition metal oxides can range from 3.5 to 7 eV and can be influenced by the structure and composition of the material, especially the stoichiometry, and the dopants presence[10].

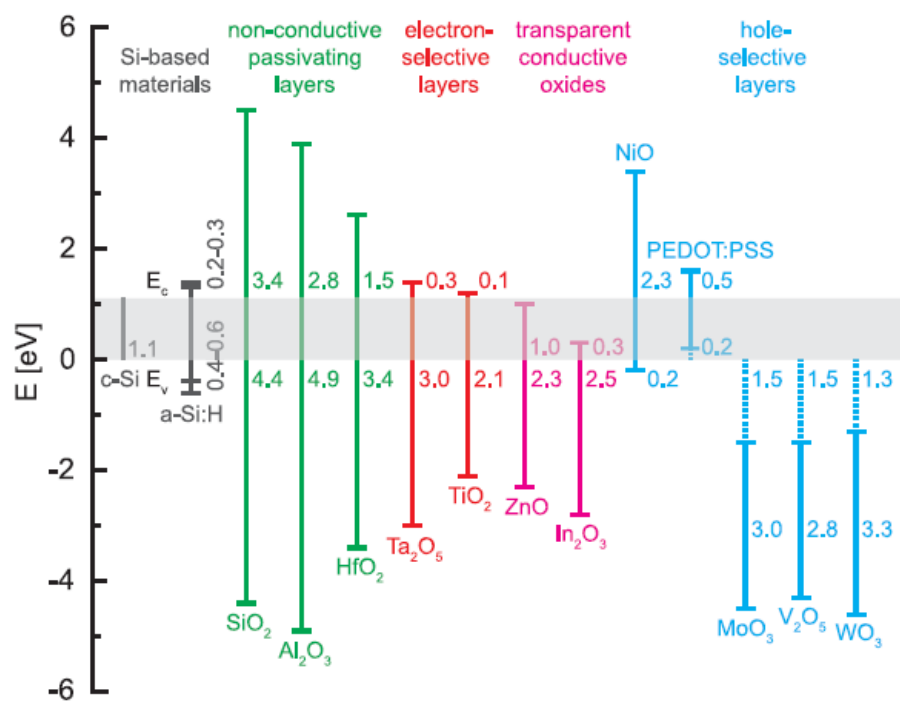


Fig.7 From Ref. [10], Conduction and valence band offsets of various materials with respect to c-Si. For materials that have a work function greater than that of c-Si (MoO_3 , V_2O_5 , and WO_3), the energetic difference between the conduction band of those materials and the c-Si valence band is shown. Note that all values should be taken as indicative only, since the exact values will depend on aspects such as the deposition method, stoichiometry, and the doping level of the material [10]

2.3.2 Hole Selective Contacts

In this section, the focus is on the hole selective contact as consolidated background introduction for the main research theme which is RF-sputtered Molybdenum Oxide (MoO_x). we present as an example the reported work in Ref.[4], where three hole selective contact TMOs materials has been studied intensively MoO_x , WO_x , VO_x [4]. In Fig.8 [4], those three materials has been shown before establishing physical contact with absorber base. Crystalline silicon n-doped layer band diagram is also shown in the same figure to highlight the energy differences between them. The most point that deserve observation in the Fig.8 is that , hole selective contact TMO's Fermi level is much lower than the c-Si one [4].

Typically, in any junction, the difference between Fermi levels induces curvature of the Energy bands. In the classical crystalline silicon junction, the doping of each zone is what determines the Fermi energy levels since the electron affinities (EA) are the same. Since Fermi level of n-type is higher than Fermi energy level of p-type, electron will diffuse from n-type side to p-type side until Fermi level is equal in both sides. Basically, band bending due to charge inversion of n-doped silicon interface represents junction electrical field in space charge region. [4]

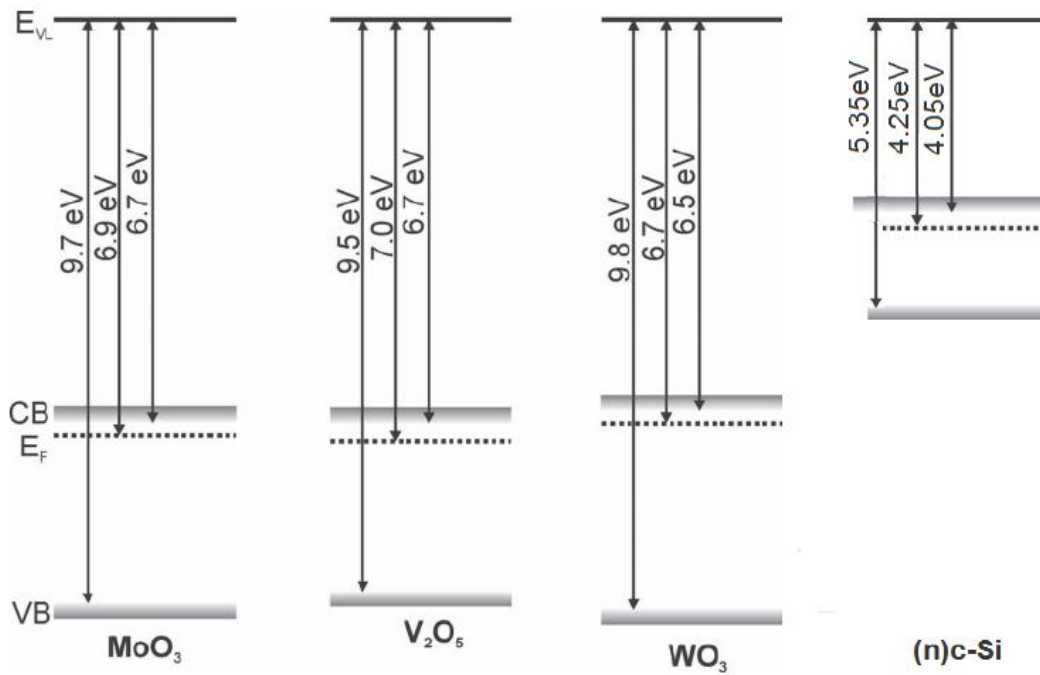


Fig. 8 Energy levels of three common used electron transport TMOs: MoO₃, V₂O₅, WO₃ and n-doped crystalline Silicon c-Si. VB and CB are the valence and conduction bands respectively, E_{vL} is the vacuum level and E_F is de Fermi energy level by Ref. [4].

Luis et al. [11] has shown their experimental work cell results for evaporated Vanadium Pentoxide (V₂O₅), Tungsten Trioxide (WO₃) and Molybdenum Trioxide (MoO₃) beside reference SHJ cell results summarized in Table.I. We can observe that in this reported work [11], cell with a-Si:H having better results than other TMOs based cells, However, in the latest research work research TMO based SHJ has already reached efficiency of 22% at over 700mV Voc.

Table.I Photovoltaic parameters obtained for the fabricated solar cells with transition metal oxides with (15 nm) layer thickness as hole- selective contacts, compared to a reference heterojunction device with a-Si:H emitter [11].

Hole contact		V _{oc} (mV)	J _{sc} (mA/cm ²)	FF (%)	PCE (%)
VO _x	TMO	606	34.4	75.3	15.7
MoO _x		581	34.1	68.8	13.6
WO _x		577	33.3	65.0	12.5
a-Si:H	Ref.	685	34.4	77.6	18.3

2.4 Electronic Transport Mechanism in TMO

In early reported research work [4], Gerling et al. showed that MoO₃ exhibited n-doped donor states. In fact, the idea is that, SHJ with TMO contact presents an n-doped layer on a n-doped c-Si wafer but it extracts holes as a p-doped layer would do. Previously, this phenomena did not have a well-demonstrated explanation [4]. Recently, in the work of Luis et al. [11], it is elucidated by considering two diodes current model, that the carrier transport mechanism in TMO/n-Si heterojunctions suggests that the dark J–V response is limited by diffusion of injected minority carriers (J_{01}) and recombination in the space-charge region (J_{02}), rather than alternative processes such as thermionic emission current [11]. This work has been experimentally studied using dark (J–V) characteristics [11]. J–V dark characteristic was measured at varying temperatures and fitted for the double diode solar cell model followed by extracting first diode current (J_{01}) and second diode current (J_{02}) for the diffusion and recombination diodes respectively. Fig.9. The thermally-activated behavior of each (J_0) is defined by a specific activation energy (E_a) as in EQ.1:

$$J_0 = J_{00} \exp(-E_a/nkT)$$

EQ.1

where (J_{00}) is the saturation current pre-factor, (kT) the thermal voltage and n - the ideality factor for each fitted diode ($n_1 = 1$ and $n_2 = 2$).

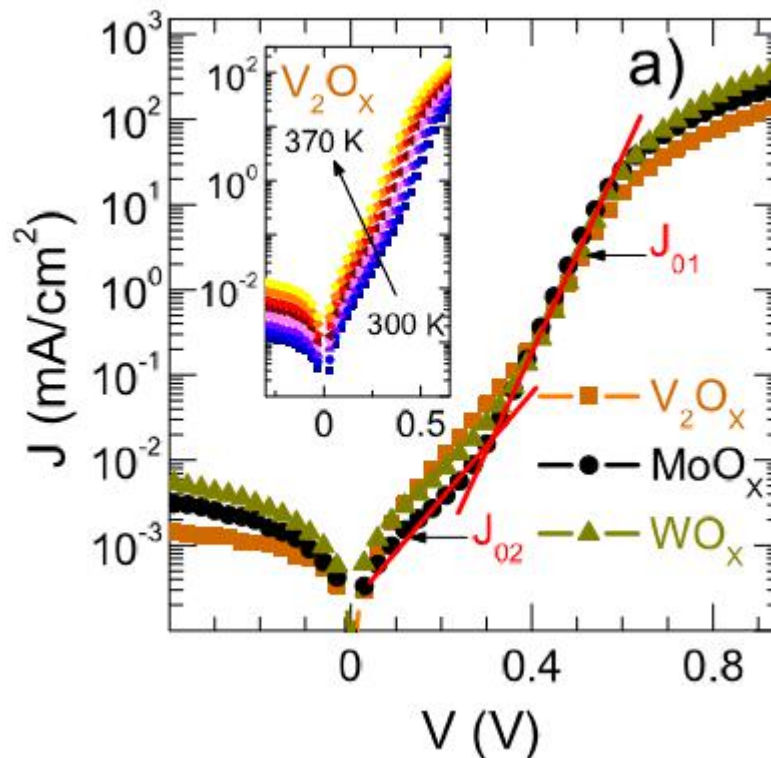


Fig. 9 a J–V characteristics were measured at varying temperatures and fitted for the double diode solar cell model by Ref. [11]

Typical Arrhenius plot in Fig. 10 (Gerling et al.) [11] obtained by fitting extracted experimental data to exponential model, the obtained activation energies for seeming to be related to crystalline silicon’s bandgap ($E_{a1} = E_{gap}$, $E_{a2} = \frac{1}{2}E_{gap}$). Based on the obtained (J_0) (E_{gap}) dependence, the classical depletion approximation was then used to analyze the TMO/n-Si heterojunction. Departing from equilibrium condition, the Fermi level difference between both semiconductors is distributed between the induced Built-In Potential (V_{bi}) across the heterojunction and the Surface Dipole (Δ) that very likely occurs at the interface as in EQ.2

$$\Phi_{MoO_x} - \Phi_{n-Si} = qV_{bi} - \Delta \quad \text{EQ.2}$$

This (V_{bi}) is expected to be mostly allocated on the silicon bulk, given the thinness of the TMO layer. As mentioned before, the effect of the V_{bi} is a pronounced band bending of silicon’s valence band up to the point of surface inversion, creating a p+ contact appropriate for hole transfer, as depicted in Fig.11 [11]. Similarly, up-bending of the conduction band creates a barrier for electrons, promoting the separation of photogenerated carriers. By assuming a strongly inverted surface potential $\psi_s = V_{bi} = 0.7$ V, negative trap charges in the TMO/n-Si interface gives a dipole of $\Delta \sim -0.5$ V, [11]

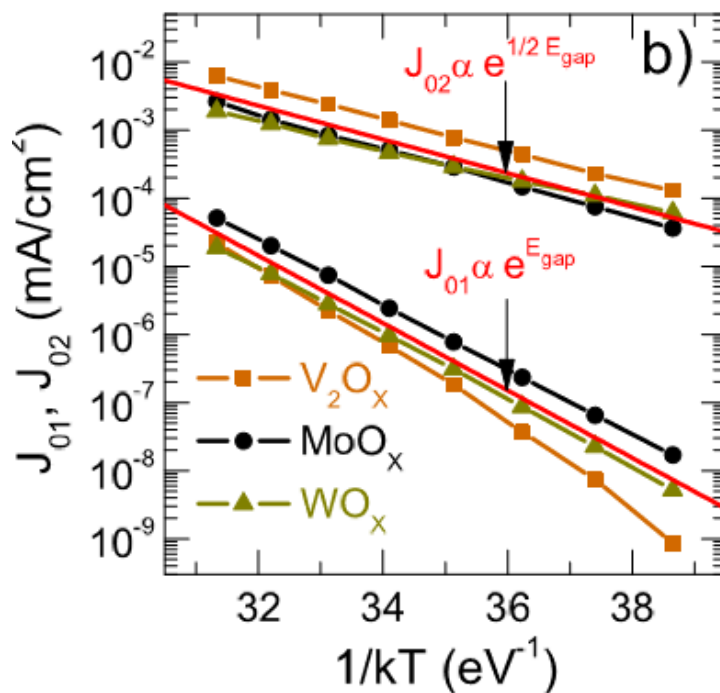


Fig. 10 Exponential fit of the Arrhenius plots for J_{01} and J_{02} by Ref.[11]

Interestingly, the presence of negative dipoles in TMOs has been previously reported by [11], as it originated from shallow O vacancies and playing an important role in energy level alignment with several organic semiconductors. Moreover, assuming such TMOs having n-type nature and relatively low density of gap states, it can be argued that the transport of photogenerated holes across the oxide bulk does not occur, but instead they recombine through trap assisted tunneling in the TMO/n-Si interface with those electrons supplied by the ITO contact [11]. In the last years, several carrier transport modeling simulations were attempted, the bottom line; while models of carrier transport can happen due to trap assisted tunneling in the TMO in Fig.11. Others showed band to band tunneling transport between a-Si:H(i) and the high work function TMO's materials[3].

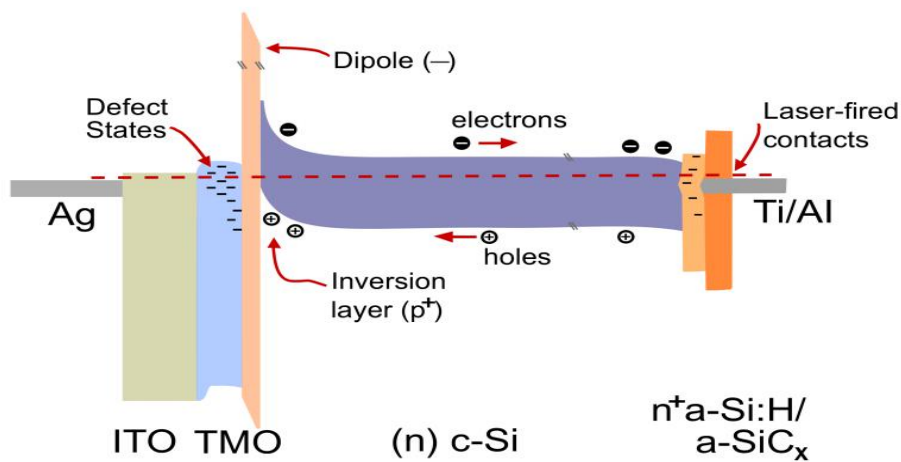


Fig. 11 Band bending of silicon's valence band up to the point of surface inversion creating a p⁺ contact appropriate for hole transfer by Ref.[11]

2.5 Molybdenum Oxide (MoO_x) as Hole Selective Contact

2.5.1 MoO_x-n-c-Si band diagram

Typically, in Molybdenum Trioxide (MoO₃) or near stoichiometric (MoO_x) electronic structure, Fermi energy level can be much lower than the one of n-type c-Si. Accordingly, the electrons of the n-type c-Si substrate (high Fermi energy level) will diffuse into the MoO_x layer (low Fermi energy level) and the bands will bend as in a p-n junction see Fig.12 [4].

In fact, it is not the same case as in a p-n junction for many reasons. One may notice that MoO₃ bands were not ideally bent and the whole depletion zone is on the c-Si. Theoretically, the proposed explanation is that since MoO_x is a thin film material with a high level of donor states the electrons that diffuse from n-c-Si remain in the first few nanometers suggesting that

MoO_x band bending is almost negligible. Nonetheless, In practice, other works represent MoO₃ junction with bent energy bands [4].

Furthermore, important aspect to comment is that in Fig.12 c-Si energy bands have been completely bent until the point where Fermi level have reached the valence band. In that sense, one can imagine just before junction establishment, difference between Fermi energy levels of both materials suggest that there is remaining energy that can not bend c-Si energy bands anyfurther. The proposed answer is that there is a surface charge density as in Metal-Oxide-Semiconductor (MOS) proportional to that remaining energy. [4].

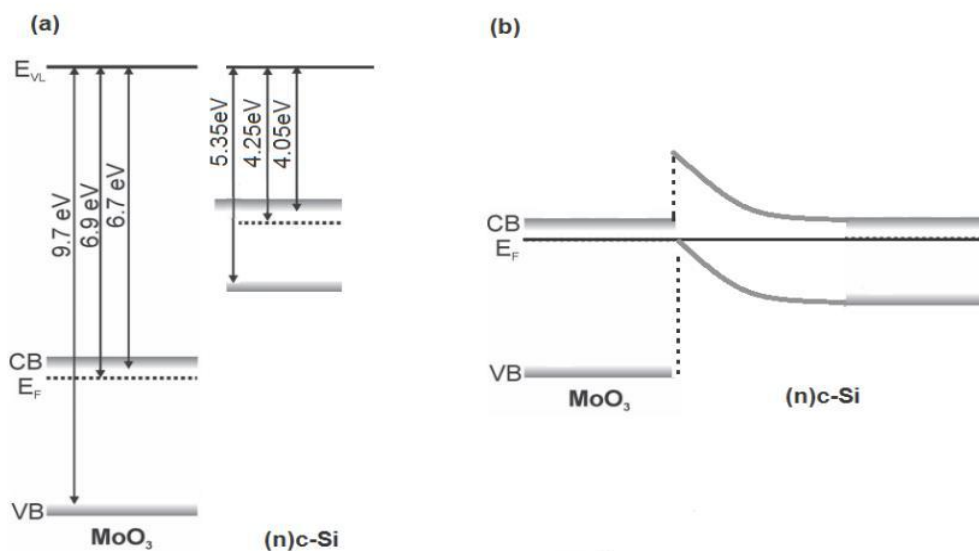


Fig. 12 Crystalline silicon p-n junction band diagram: [a] isolated condition and [b] forming a junction from Ref. [4]

2.5.2 MoO_x oxidation states and high work function origin

Basically, when MoO_x defined in crystal structure context, Molybdenum has two main oxide forms, namely, molybdenum trioxide (MoO₃) and molybdenum dioxide (MoO₂) [12]. Bulk molybdenum trioxide (MoO₃) is a layered material with an orthorhombic crystal structure, while MoO₂ has a monoclinic structure which deviates only slightly from the rutile structure. In fact, due to enthalpy difference between two different oxides, MoO₃ is rather easily reduced and forms at least well known eight stable Magne´li phases in the intermediate region between MoO₃ and MoO_{2.6,7}. All the Magne´li phases in the MoO_x system have crystal structures with orthorhombic, monoclinic or triclinic symmetry when it measured with X-ray Diffraction XRD. MoO₃ is an extreme case of MoO_x optical and electrical properties, MoO₃ is a

transparent and insulating material, whereas other extreme case is MoO_2 which takes optically a brownish violet color and electrically metallic conductor form [12].

Remarkably, Mark et al.[13], investigated the correlation between work function and oxidation states of several TMOs. In our case, if we take the plot of MoO_x work function versus cation oxidation as shown in Fig.13. This plot demonstrates that a general trend exists between transition metal cation nominal oxidation state and work function. It is worth to observe that from Fig.13 the scatter is caused by several factors such as oxide thin films thickness. It is remarkable to mentioned that work function depends on oxide thickness, because of defects near the metal/ metal-oxide interface. After a certain thickness, work function plateaus at a maximum value. Thus, oxide films must be sufficiently thick to experimentally obtain reproducible values. Another possible reason for scattering in the data points is also a measurement of oxidation state precision [13].

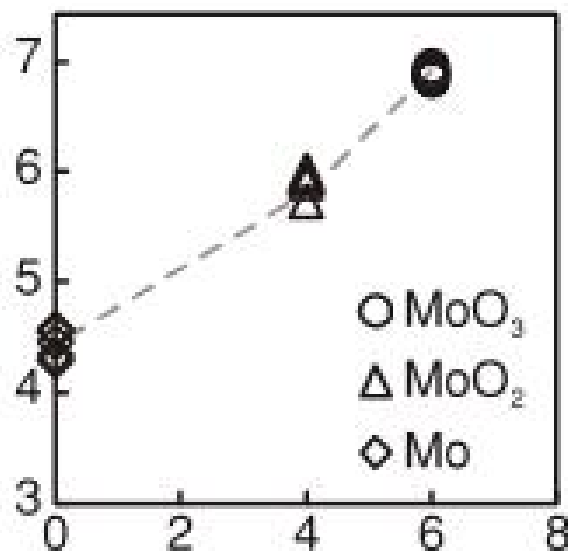


Fig.13 Plots of work function versus nominal average oxidation state of metal atoms in MoO_x by Ref.[13].

2.6 Reported results of solar cell with MoO_x contacts

MoO_x films were recently also integrated into SHJ devices using evaporation technique so as to replace the p-a-Si:H layers, resulting in clear optical gains, typical MoO_x cell results shown in Table.1. However, Jonas et al [14] argued that in their reported results for MoO_x , FF remained below 70%, with increasingly pronounced S-shaped illuminated J-V curves when increasing MoO_x film thickness, indicating a hole collection issue despite its argued appropriate

work function [14]. Importantly, MoO_x films are sensitive to air and oxygen exposure, as well as to temperature or - in case of- RF-Sputtering treatment which might impact solar cell performance due to degradation mechanisms arose from sputtering damage [14].

2.6.1 Annealing impact on MoO_x contacted solar cell

As for the impact of annealing on device level, same experiment setup fabricated for solar cells featuring either MoO_x or standard p-aSi:H hole extraction layers [14]. The cells were metalized by using screen-printing, followed by annealing at the lowest possible temperature, the reason for that is to evaporate the solvents contained within the silver paste. Once this step finished, the reported cells were subsequently annealed at 130 °C, 180 °C, and 200 °C in steps of 15 min. For the reference cell, Fig. 14(a) confirms that increasing the annealing temperature up to 200 C improves the device performance (FF improves from 75.4% to 77.1%), which is attributed to the improved metal conductivity as well as to improved passivation. However, the dramatic performance deterioration is observed for annealing above 130°C with pronounced S-shape which is strongly suggesting the appearance of a hole-blocking barrier, Fig.14 (b) [14]. Remarkably, Geissbühler et. al (s) assumed a possible cause for hole-blocking barrier is MoO_x/TCO interlayer, which thickens with annealing. Interesting observation from the reported experiment is that the occurrence of the S-shaped curves was found to be independent of the annealing ambient (air or N₂- purged) [14].

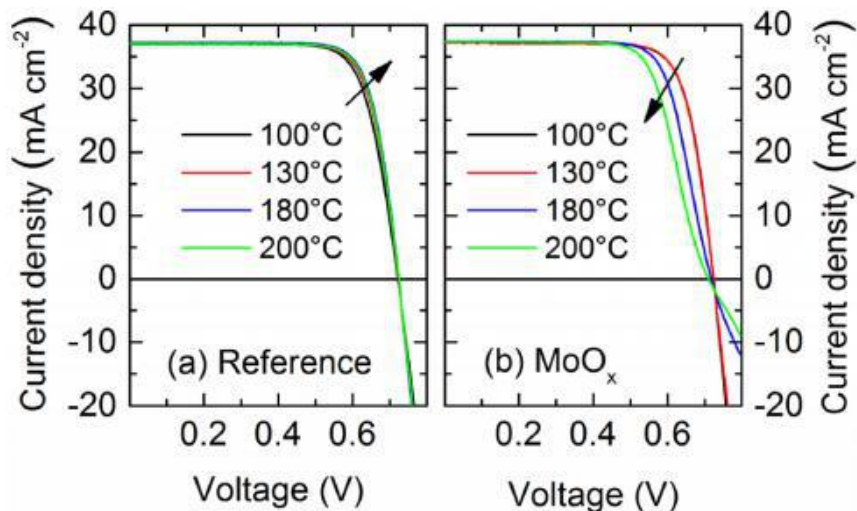


Fig. 14 Light J-V characteristics of (a) reference SHJ structure and (b) MoO_x-based SHJ solar cells after post-processing annealing at various temperatures. Measurements were taken at room temperature by Ref-. [14].

2.7 Sputtering Process

Sputtering is a widely used industrial technique in thin-film processing. Such films may be sputtered from alloy targets, co-sputtered from different sources, or be reactively sputter deposited. Sometimes such compound films may be produced by reactive sputtering [15].

Reactive sputtering is a very complex nonlinear process and often exhibits hysteresis effects. thus control requirements are even more rigorous. [15]. Degree of combining a high deposition rate and true compound stoichiometry of the deposited film turn out to appear as contradicting desires.

The hysteresis effect is one of the key problems in experimental reactive sputtering systems. It can be considered as an implication of process instability through measurement of hysteresis width. In the following treatment Fig. 15, a difference in increasing and decreasing the supply of the reactive gas illustrated can be explained with more gas is consumed for compound formation during the increase sequence of the reactive gas supply, the partial pressure of the reactive gas remains at a very low level until reaching the upper limiting value of the hysteresis width. During a decrease of the supply of the reactive gas, the partial pressure remain high while lowering reactive gas flow until reaching the lower limiting value of hysteresis [15].

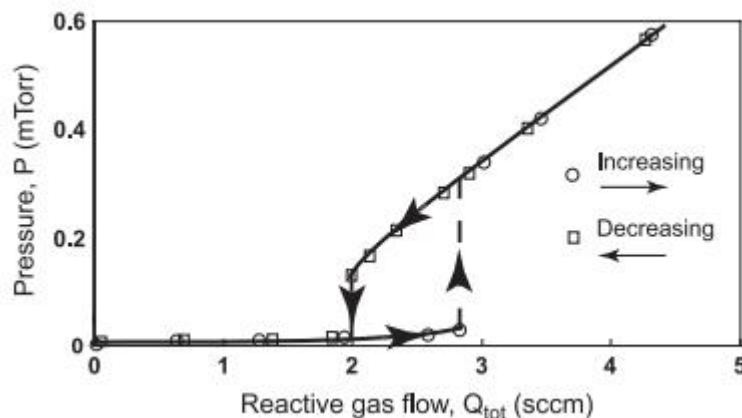


Fig. 15 The partial pressure, P , of the reactive gas from Ref. [15]

The main idea for reactive sputtering film composition prediction lies in the commonly accepted heuristic treatment and is frequently referred to as Berg's model [15].

Berg model [15] predicts that the shape of the processing curves depends strongly on the size of the effective target area. Work of Berg et al. [15] demonstrated that there hysteresis is less pronounced for a small size target area under these processing conditions, however, that

the critical target size for hysteresis-free operation also depends on several other processing parameters mentioned in Ref.[15].

2.8 Sputtered MoO_x for solar cells

Several researches have reported TMO contacted SHJ solar cells with satisfactory results. One of the famous work investigated molybdenum oxide (MoO_x) thin films synthesized by reactive dc magnetron sputtering by Pachlhofer et.al . [16]. All results of MoO_x is function of varying oxygen/argon gas flow ratio. In general, it can be concluded that microstructure and properties of molybdenum oxide thin films can be adjusted by varying the oxygen/argon gas flow ratio [16]. Shortfall of silicon heterojunction solar cells reported by Julia et al. is the passivation damage and (Voc) loss induced by sputtering and e-beam evaporation [16].

Measurements of the electrical resistivity of the samples indicated that the MoO_x films at room temperature change from electrically conductive to insulating for different p[O₂] used during deposition. As illustrated in Fig. 16, the resistivity value of the film deposited with p[O₂]=0% is comparable to metallic MoO With increasing p[O₂], the resistivity of the MoO_x films increased monotonically up to a value 5 orders of magnitude higher for the film deposited with p[O₂]=90%, dominated by the Mo⁶⁺ cations, with respect to that obtained for the Mo and Mo dominated films. The sample grown at p[O₂] =100% is characterized by an insulating behavior as expected for a fully oxidized MoO₃ thin film [16].

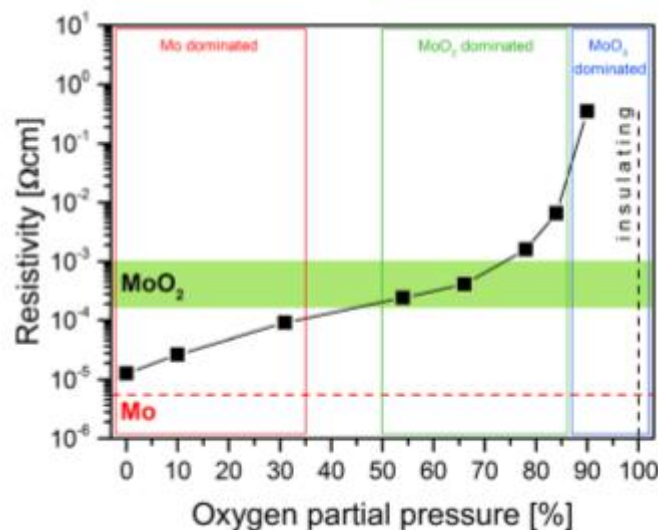


Fig.16 Electrical resistivity of the synthesized MoO_x thin films at room temperature as a function of the oxygen partial pressure used during deposition. Regions of different MoO_x based phases are indicated. Reference values of the electrical resistivity of Mo and MoO₂ from literature are also included [16].

Fig.17 shows another reported result by Myeong et al. [12], for the composition variations of the MoO_x films as function oxygen partial pressure, which were determined from Rutherford Back Scattering (RBS) characterization method, as a function of the sputtering pressure at various O_2 contents. The O/Mo atomic ratio of the MoO_x films decreased with decreasing sputtering pressure at the same O_2 content. From Berg Model [15], this reduction can be explained by considering the deposition mechanism of reactive sputtering due to more target poisoning occurs as results of an increased number of O_2 molecules with increasing sputtering pressure at the same O_2 content. Thus, as reported by the author (s), MoO_x molecules with best band bending -so far- is having approximate O/Mo atomic ratio of around 2.85 [12].

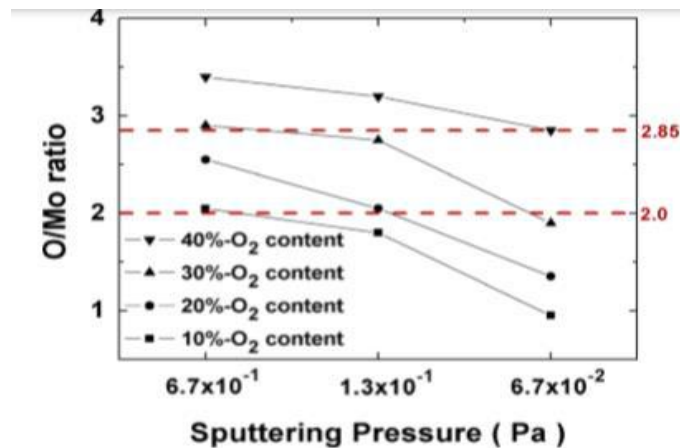


Fig.17 Mo ratio of the post-deposition annealed (PDA) MoO_x films, which was analyzed by RBS, as a function of the sputtering pressure at O_2 contents of 10, 20, 30, and 40% from Ref.[12].

3. Chapter Three: **Experiment Setup and** **Characterization Tools**

3. Chapter Three: Experiment Setup and Characterization Tools

This research work aims to find the optimum sputtering deposition and post deposition physical conditions for sub-stoichiometric Molybdenum Oxide (MoO_x) for hole selective contact for silicon solar cell application. A schematic cross-section view for the target structure is provided in Fig.18 [17]. The main distinction from the thermal evaporated MoO_x lies the deposition technique and post-deposition annealing process conditions.

Hence, the entire experiment protocol comprises; pre-deposition wafer cleaning, deposition process i.e. sputtering, post-deposition conditioning process and characterization measurements.

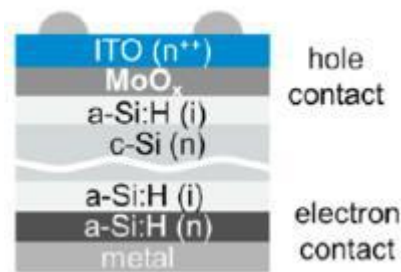


Fig.18 Typical MoO_x over Reference structure on flat mirror polished c-Si [17]

3.1 Pre-deposition wafer cleaning

Pre-deposition process typically involves c-Si substrate cleaning and/or c-Si with deposited amorphous silicon substrate preparation with diluted hydrofluoric (HF) acid solution so as unwanted surficial oxide being removed prior deposition process [16].

3.1.1 Contamination sources and prevention method

Contamination defined as a substance that causing uncontrolled/unwanted variations in: - device electrical and mechanical performance and process performance as well. Contamination on the wafer surface may lead to device failure and drastic yield reduction [18]. In solar cell the most factor that being influenced by the impact of contamination is low minority's carrier lifetime [19]. Practically, contamination can be transferred between wafers (front-side/backside) and tools (transport modules, chamber walls, wet processing media) [19]. Essentially, surface contaminant films and particles can be classified as molecular compounds, ionic materials, and atomic species. Molecular compounds are mostly particles or films of condensed organic vapors such as components from plastic storage containers. Ionic materials comprise cations and anions, mostly from inorganic compounds that may be physically or

chemically adsorbed ions such as sputtering chamber's wall. Atomic or elemental species comprise metals, such as gold and copper. An example of atomic contaminant is silicon particles or metal debris from equipment [19]. To prevent contamination source, long time process experience has been built up in this field to address wafer contamination [19]. During our experimental work, cross-contamination is prohibited according to the specific contamination study on each contamination source such as chemical elements and experimental working zone classification.

3.2 Deposition process: RF-sputtering tool parameters

Following pre-deposition process, wafers must be fixed on sputtering tool wafer carrier with Kapton tape prior RF-sputtering process. MoO_x sputtering takes place in multi sputtering elements (Nimbus310) sputtering tool Fig. 19 [20] Nimbus 310 is capable to provide the following specified basic process conditions Table.1. Most of the physical controlling parameters can be minimized and maximized, however they are being optimized according to the best practice from former tool users.

Table .2 Nimbus 310 controllable process parameters [20]

Controlling Parameter	Minimum	Maximum
Power (W)	30	5000
Argon flow (sccm)	0	200
Oxygen flow (sccm)	0	100
Basic Pressure (mtorr)*	1E-5	5E-6

Molybdenum (Mo) is one of sputtered target can be loaded on Nimbus310 along other optional targets in five angle clustered type sputtering material holder. Oxygen introduced through mass flow controller (MFC) to produce reactively sputtered MoO_x on silicon substrate. Right after plasma stabilization and sputtering process completion, post-deposition annealing is necessary for damage recovery.

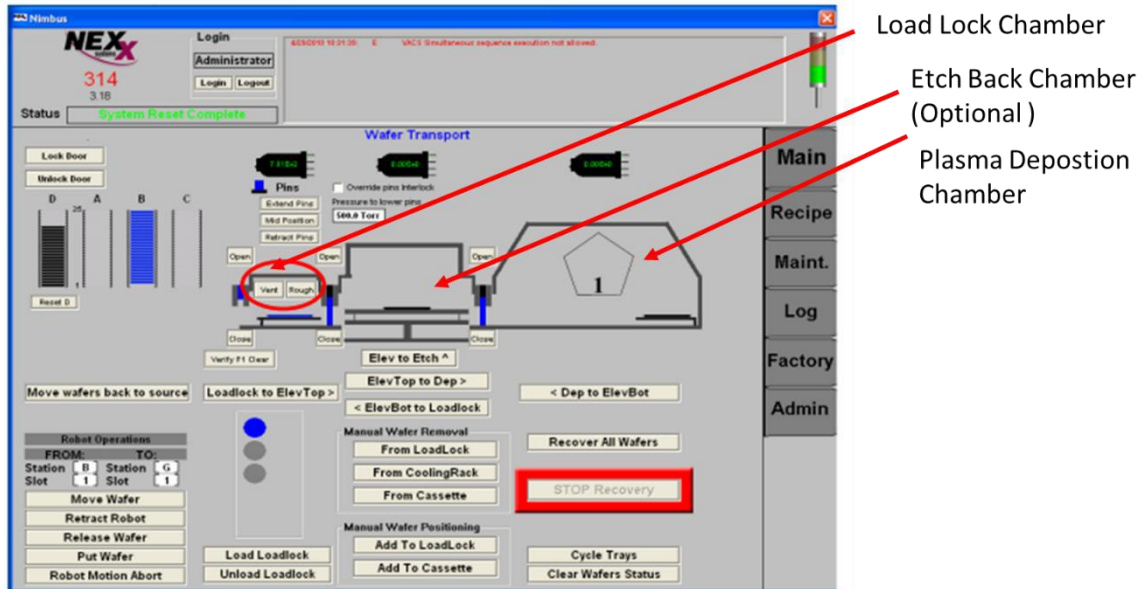


Fig. 19 Main screen of the NimbusXP sputtering tool along with load lock, etch back and RF-sputtering plasma deposition chambers ringed in red [20]

3.3 Post-deposition annealing process

Annealing of MoO_x on referenced structure wafer samples is performed in rapid thermal annealing (RTA, Heat Pulse) process based tool in nitrogen (N_2) environment up to specific temperature (up to 160°C for one hour) without causing loss of reference structure passivation [21]. The temperature control in different optional annealing gas atmosphere is done by thermocouple for temperatures below 700°C . The system operates at atmospheric pressure while the substrate lays horizontally on three quartz pins [21].

3.4 Sample characterization and measurements

Sample measurement can be classified into film analysis, electrical and structural analysis. Necessary film analysis is film thickness, X-Ray Photoelectron Spectroscopy (XPS) measurement and elastic recoil detection analysis (ERDA) measurement. Electrical analysis involves; photo-luminescent (PL) measurement, SunsVoc measurement and capacitance-voltage (C-V) measurement. Finally, Structural characterization in turn include Transmitting Electron Microscopy (TEM).

3.4.1 Film Analysis

3.4.1.1 Film Thickness

As shown in Fig. 20, film thickness was measured with surface profiler (DektakXT®), which is an advanced thin and thick film step height measurement tool. The stylus profiler version where our experimental work is going on provides a step-height repeatability up to 6nm [22].



Fig. 20 DektakXT® stylus profiler tool where main parts are clearly indicated with arrows [22]

3.4.1.2 XPS Analysis

XPS is for electron spectroscopy for chemical analysis. The main function is used to retrieve chemical state of elements at the wafer surface with angle-resolved analysis. Many models can be used to understand and stand and analyze photo-electron physical basis, however, three steps model in Fig. 21 used to analyze XPS data. However, XPS can be used in depth profile mode, where repeated cycle of Ar sputtering and analysis composition analysis can be performed on wafer sample. An XPS spectrometer is commonly constituted from an X-ray source, an electron analyzer-detector; a sputtering source and a charge neutralization source. For our samples case, samples tested with various angle resolved modes as in Fig.22. [23] [24].

Physical basis for XPS is X-ray beam illuminates a sample from which electrons are ejected by the photoelectric effect. The kinetic energy of the ejected electrons is then analyzed. Parting from energy of the X-ray and of the ejected electron are known with Electron Analyzer, the

binding energy of the electron then can be determined, which leads to the identification of the elements from which the electron originates.

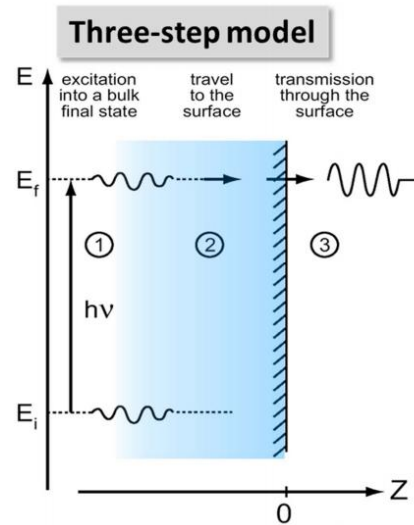


Fig.21 Schematic spatial energy representation of three step model of the photoelectric effect[23].

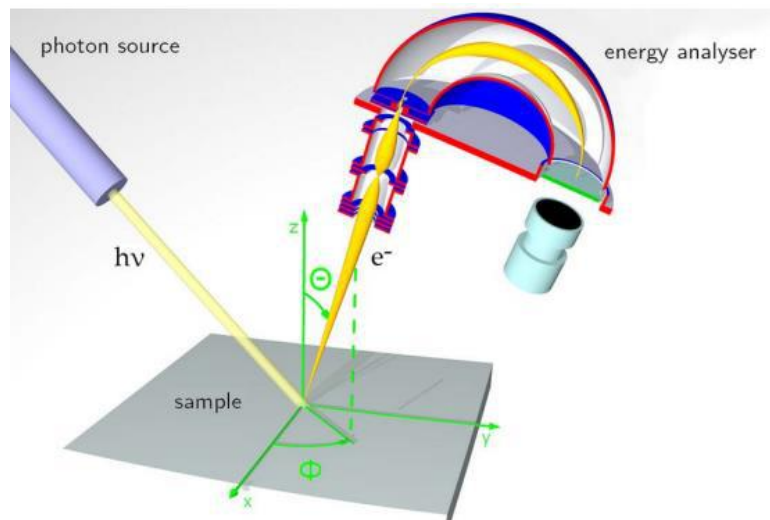


Fig.22 Schematic representation from an angle resolved XPS spectrometer where electron energy and momentum are measured for XPS distribution [23].

As far it may concern this research, typical evaporated MoO_x oxidation state is determined by XPS. For instance, typical oxidation state reported in Greiner et, al. [13], the main Mo3d

orbital peak spotted approximately at 232.50 eV is from higher oxidation state Mo6 + followed by Mo5 + appears at ≈ 231.5 eV Fig 22 (e). Standard calculations after fitting peaks data to Gaussian model and integration over the Mo 3d and O1s areas is used to determine the O-vacancy concentrations [13]. In the same work [13], reported in addition to XPS measurement, UPS spectrum of MoO₃ Fig.23 consists of a distinct O [2p] band, centered at binding energy ≈ 3.5 eV . The presence of [Mo5 +] cations (i.e. shift from high oxidation states to the lower oxidation states) causes filling of the Mo [4d] band due to extra electron left from oxygen, which gives rise to a distinct peak centered at binding energy ≈ 1 eV . In Fig.23 (b–d), defects were introduced using noble gas ion sputtering demonstrate how the secondary electron cut-off (i.e. used for determining work function) and the UPS valence-band spectra and of MoO₃ change as the O-vacancy concentration increases. The correlation between O-vacancy in previous graph is demonstrated for MoO₃ work function starts off at ≈ 6.7 eV for nearly stoichiometric MoO₃ and it decreases as O-vacancy concentration increases. Meanwhile, the O [2p] valence band shifts to higher binding energy and a new occupied state appears within MoO₃ bandgap, labeled 'd' in Fig.23 [13].

Another advantage of XPS measurement is chemical analysis which arise from small variation of the binding energy on the chemical state of the elements. In nutshell, XPS for thin layers (<4-5 nm), the composition depth profile can be calculated through a complex mathematical procedure. However, the results obtained by this method should always be taken with caution.

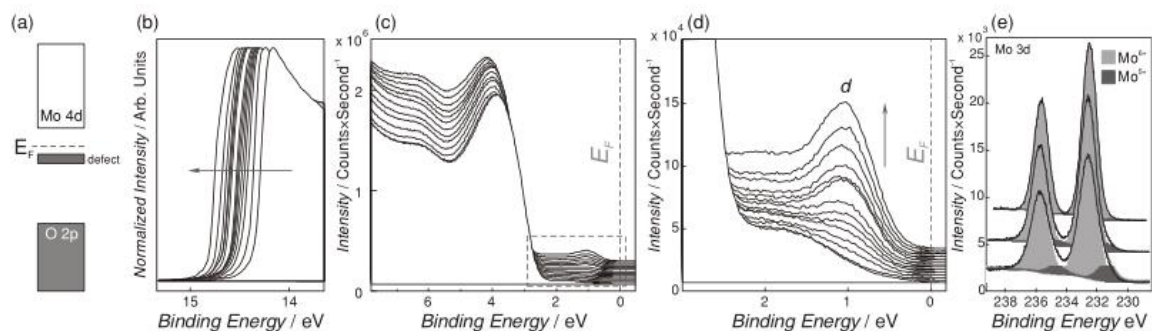


Fig. 23 From Ref. [13] (a) Energy-level schematic of O-deficient MoO₃, with the Fermi level E_F , O 2p band, Mo 4d band, and defect band indicated. (b–d) UV photoemission spectra of MoO₃ as oxygen vacancies are introduced: (b) secondary-electron cut-off, (c) valence band, and (c) expanded view of the shallow valence features. The gap state resulting from the oxygen vacancy defects is labeled d. (e) Mo3d XPS spectra of MoO₃ as the oxygen vacancy concentration is increased [from top to bottom]. The peak components from (Mo6+) and (Mo5+) are indicated [13].

3.4.1.3 ERDA Analysis

Elastic recoil detection analysis (ERDA) is a technique to analyze the chemical composition and elemental depth profile of thin films. ERDA is a partially destructive analysis based on detected ejected ion from the target sample (columbic interaction) by projectile atoms with a sensitivity of about 1 atomic % and a depth resolution of 10 nm in wafer sample and used to reconstruct the elements present in the sample and the distribution of these elements in depth (Fig.24) [24]. ERDA provides information on the composition and the distribution of the different elements. Unlike XPS, ERDA is mostly suited to detect the light elements (from H to Mg) in a matrix [24].

In this technique, heavy ions (for example Cl^{4+}) are accelerated to a high energy using a (2 MV) particle accelerator by steering magnets are used to direct the energetic particles (typically 6 – 10 MeV) under a glancing angle (between 5 and 20 degrees) towards the sample Fig.24 [25]. The kinetic energy and speed (time-of-flight) of each atom reaching the detector (i.e. typically at 40° from the forward direction) is extracted to evaluate mass of each atom detected in the sample as function of flight time along with concentration depth profiling as shown in Fig.25 [24].

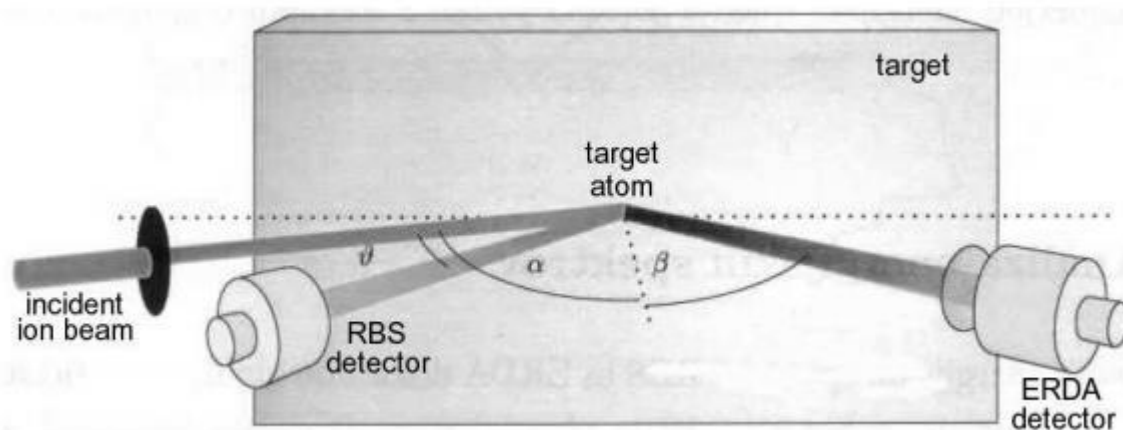


Fig.24 ERDA basic setup shows incident high energetic projectile eject ion from target sample and detected with ERDA detector, likewise the same principle with RBS which detect elastically scattered ion from target from Ref.[25]

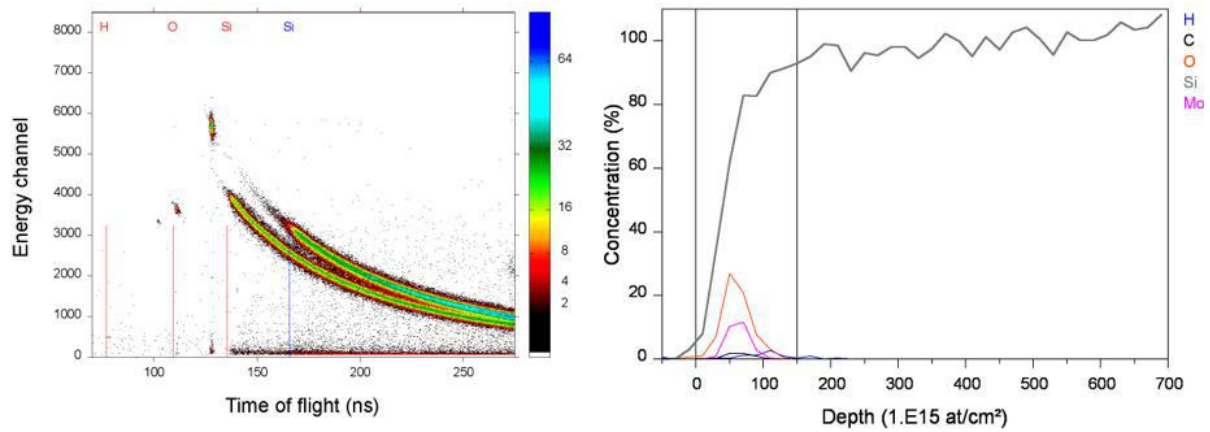


Fig. 25 (a) energy and time-of-flight for 10 nm MoO_x/native SiO₂ on c-Si (b) Depth profile of atomic concentration for the same sample-By IMEC [24]

3.4.2 Electrical analysis

3.4.2.1 Photo-luminescent (PL) measurement

Lifetime measurement is a technique used to give information about the low defect densities in semiconductors in terms of carrier life time. Typically, the simplest calculation of the effective life time is contribution of three carrier recombination techniques radiative, Auger and Shockley-Read-Hall recombination mechanisms as follows [28]:

$$\frac{1}{\tau_{eff}} = \frac{1}{\tau_{rad}} + \frac{1}{\tau_{Auger}} + \frac{1}{\tau_{SRH}}$$

EQ.5

Where τ_{rad} is radiative recombination time, τ_{Auger} is auger recombination time (The energy of the recombining electron-hole pair is transferred to another carrier) and τ_{SRH} is Shockley-Read-Hall recombination time (Recombination through deep local trapping centers (crystal defects and contaminants in the bulk, dangling bonds at the surfaces)).

One of the potential and useful methods for measuring carrier lifetime is photo-luminescent measurement technique. For such case, BT Imaging tool is used to conduct photo-luminescence (PL) and Electroluminescence (EL) measurement of both solar wafers and solar cells respectively. Another interesting measurement parameter provided by BT-imaging tool used to assess passivation quality is quasi steady state photoconductance (QSSPC) minority carrier lifetime as function of minority excess carrier density [28]

- PL Process description

As shown in Fig.26, simple explanation PL imaging basis is focused steady state excitation laser leads to the generation of excess carriers which will recombine possibly by different recombination mechanisms: Auger, Shockley-Read-Hall and radiative recombination . By referring to the specific recombination mechanism, infrared camera registers the radiative recombination coming from the device under test, resulting in a picture with bright and dark regions. A relation can be established between bright regions (high minority carrier lifetime) and other darker regions (low minority carrier lifetime) in terms of PL count [28].

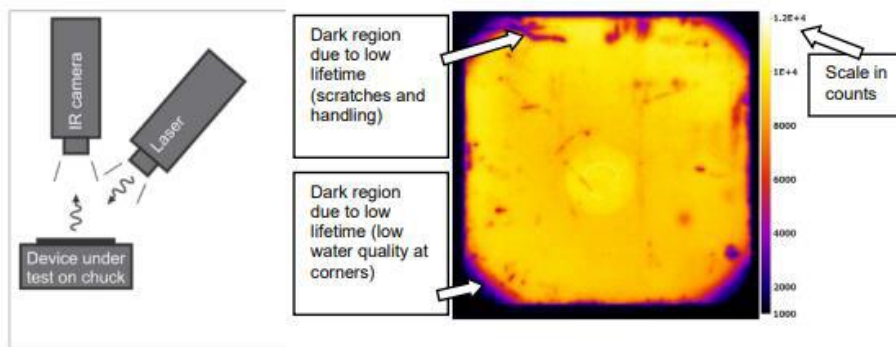


Fig.26 left is PL imaging setup and right is typical PL image where the PL scale in the far right side of the figure by Ref. [28]

- QSSPC

The sole difference in the QSSPC (see Fig.27) from PL lies in the light pulse which varies slowly in comparison with the minority carrier lifetime in the wafer in order of $(\mu s - s)$ where equilibrium excess carrier density in the wafer is reached at each illumination level of the slowly varying light pulse [28]. From the measured illumination intensity at each illumination level, the generation rate can be calculated as follows:

$$G = P_{ill} \cdot \frac{(1-R-T)}{W} \quad \text{EQ. 6}$$

with G ($\text{Cm}^{-3} \cdot \text{s}^{-1}$) the generation rate, P_{ill} ($\text{Cm}^{-2} \cdot \text{s}^{-1}$) the illumination intensity, R and T the reflectance and transmittance of the wafer and W (cm) the thickness.

The aforementioned calculation is accompanied by calculations of effective life time (τ_{eff}) as function of carrier density Fig.27 , excess carrier calculated with adoption of RF bridge in the wafer chuck which inductively measures the resistivity of the wafer[28]. Then by calculating

effective conductivity from resistivity, effective excess carrier density can be calculated according to the following equation:

$$\Delta n = \frac{\Delta \sigma}{q(\mu_n + \mu_p)} \quad \text{EQ. 7}$$

with Δn [Cm^{-3}] the excess carrier density, $\Delta \sigma$ [Cm^{-3}] the change in conductivity of the wafer resulting from illumination, q [C] the elementary charge and μ_n and μ_p [$\text{cm}^2 \cdot \text{V}^{-1} \cdot \text{s}^{-1}$] the electron and hole mobilities[28].

In the QSSPC, the resistivity is measured multiple times after the short light pulse, while the excess carrier density decreases. The minority carrier lifetime for each excess carrier density can be calculated as follows:

$$\tau_{eff} = \frac{\Delta n}{G - \frac{\partial \Delta n}{\partial t}} \quad \text{EQ.8}$$

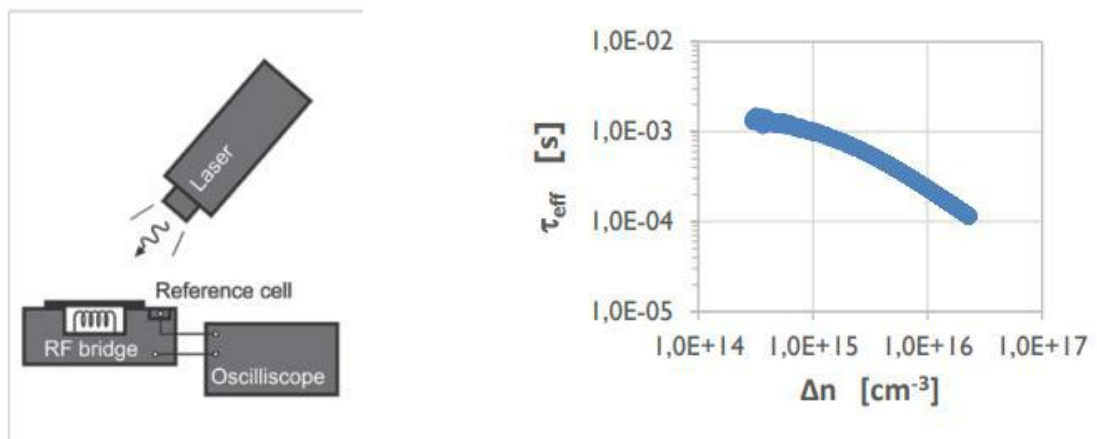


Fig.27 Left is QSSPC typical setup and right is the typical measurement result By IMEC[28] Implied- V_{oc} calculation can be inferred from Quasi-Steady-State-Photoconductance (QSS-PC). By measuring the average excess carrier concentration. Assuming the carrier concentration is constant through the base, implied V_{oc} can be calculated as follows.:

$$\text{Implied } V_{oc} = \frac{kT}{q} \ln \left(\frac{n N_A}{n_i^2} \right), \quad \text{EQ.9}$$

where n is the minority carrier concentration at the junction edge and n_i is the intrinsic carrier concentration at 25°C. The base doping, N_A , has a strong effect on Implied- V_{oc} and so must be measured on each wafer. The base resistivity is determined using the same RF system as for the QSSPC measurement [29].

- Calibrated PL imaging

While the first PL image is considered as uncalibrated image, by Comparing QSSPC value for the calculated excess carrier density to the photon flux measured by the camera from the same region of the wafer, calibrated version of PL is obtained (see Fig.28) which allows to calculate the calibration constant of the device as follows:

$$\Phi_{camera} = C_{cal} \cdot B \cdot \Delta n \cdot (N_{D/A} + \Delta n) \quad \text{EQ.10}$$

with Φ_{camera} [$\text{Cm}^{-2} \cdot \text{s}^{-1}$] the photon flux on the camera, C_{cal} the calibration constant, B [$\text{Cm}^3 \cdot \text{s}^{-1}$] the radiative recombination coefficient (material constant), Δn [Cm^{-3}] the excess carrier density and $N_{D/A}$ [Cm^{-3}] the bulk doping density[28].

Knowing the calibration constant of the wafer, the excess carrier density can also be calculated in the other regions of the wafer, based on the photon flux measured by the camera for those other regions. Thus, excess carrier density in each region of the wafer and the generation rate, the minority carrier lifetime can be calculated in each region which gives realistic and more detailed PL image for the specific sample under measurement .

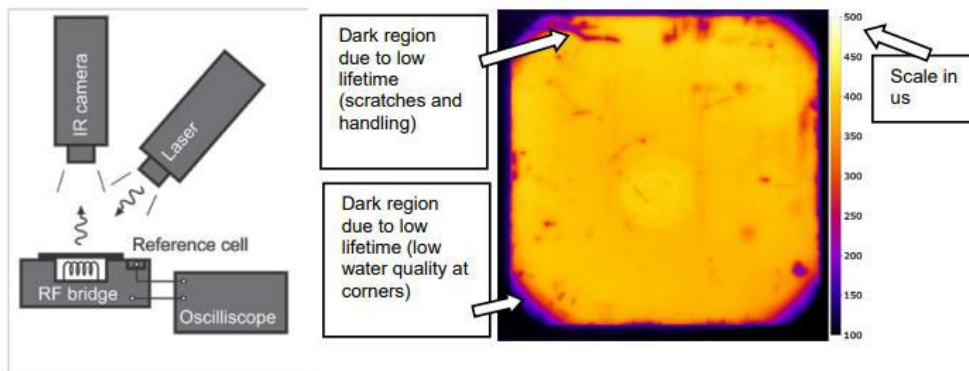


Fig.28 Calibrated PL imaging setup for sample under measurement (left) and typical calibrated PL image (right) by IMEC [28]

3.4.2.2 Open Circuit Voltage Measurement (SunsVoc)

SunsVoc is measurement technique used to reflect the dominant recombination mechanisms in solar wafer as it does not require complete cell in the case of IV measurement where

sample area factor is required. By using a combination of Implied- iV_{oc} measured using QSSPC and V_{oc} obtained using Suns- V_{oc} techniques (Fig.29), contact performance can be evaluated and compared with limiting factors which might be loss of passivation or loss of selectivity [29].

SunsVoc SINTON testing tool is used widely with a lamp spectrum approximating AM (1.5) to directly measures V_{oc} as a function of the light intensity, typically from a few suns to just below 0.1 suns [29]. Since it is a direct electrical measurement with an electrical contact (without the effect of series resistant), the V_{oc} measured at one sun should exactly match that from an IV tester assuming that the cell temperature is constant and that the spectrum of the lamp is similar. From EQ. 11, junction ideality factor 'm' can be interpreted and extracted after measurement:

$$suns \cdot J_{sc} = J_0 \exp\left(\frac{qV_{oc}}{mkT}\right), \quad \text{EQ. 11}$$

where suns is the light intensity measured by SINTON measurement tool, J_{sc} is the cell short circuit current at one sun and is a constant for a particular cell, V_{oc} is the open circuit voltage and is a function of light intensity, J_0 is the dark saturation current and kT/q is thermal voltage (25.69 mV at 25°C).

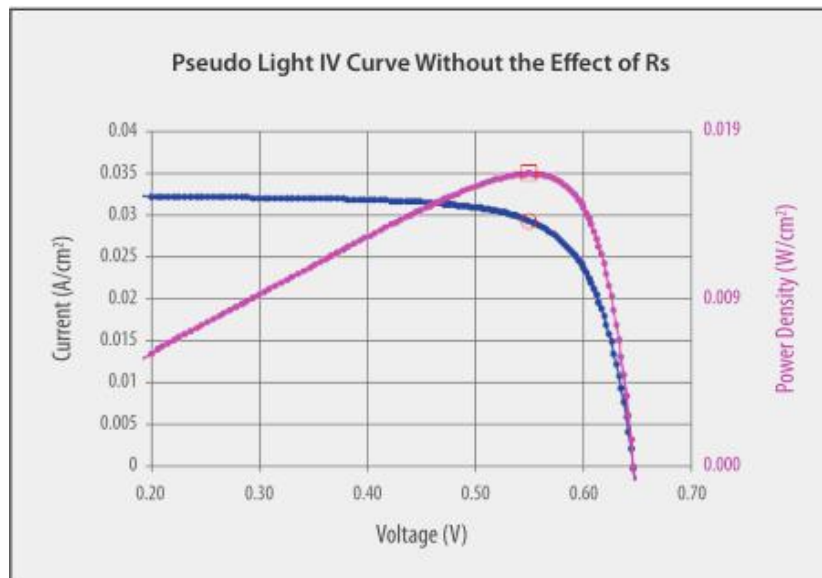


Fig.29 Suns-Voc and power density data displayed in the form of an illuminated- IV curve By IMEC[30]

3.4.2.3 Capacitance-Voltage Measurements

By definition, capacitance represents change in charge (Q) in a device that occurs when it also has a change in voltage (V) as in EQ.12 as follows: [31]

$$C \equiv \frac{\Delta Q}{\Delta V} \quad \text{EQ.12}$$

It is common practice is to apply a small AC voltage signal (millivolt range) to the device under test, and then measure the resulting current, by Integrating the current measurement over time to derive charge Q and then calculate C from Q and V. Employing Keithley measurement tool, C-V measurements in a semiconductor device are made using two simultaneous voltage sources: an applied AC voltage signal (dV_{ac}) and a DC voltage (V_{dc}) that is swept in time, as illustrated in Fig.30

The magnitude and frequency of the AC voltage are fixed; the magnitude of the DC voltage is swept in time. The purpose of the DC voltage bias is to allow sampling of the material at different depths in the device. The AC voltage bias provides the small-signal bias, so the capacitance measurement can be performed at a given depth in the device [31]

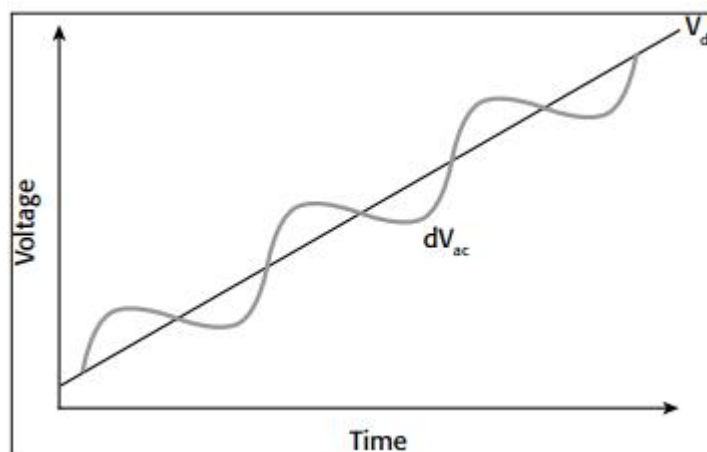


Fig.30 AC and DC voltage of C-V Sweep Measurement [31]

For semiconductor, plots of $1/C^2$ versus V yield the doping density [32] however, the same concept is used for obtaining built in potential. The value of the built-in voltage V_{bi} or flat band voltage V_{FB} of the junction is found at the intersection of the $(1/C^2)$ line with the horizontal axis. From Fig. 31 and EQ.13, $1/C^2 = 0$ when $V = -V_R = V_{FB}$ [32]

$$1/C^2 = 2(V_R + V_{bi})/q\epsilon N_B \quad \text{EQ.13}$$

Where C is the capacitance (pF), q is the elementary charge (C), N_B is the base doping (Cm^{-3}), V_{bi} or V_{FB} is the flat band voltage (V) which is defined as the gate voltage required to make the energy bands in the semiconductor flat up to the semiconductor -dielectric interface[32] and V_R is bias voltage (V). The latter is critical parameter for determining band bending which in turn is an indication of MoO_x layer work function.

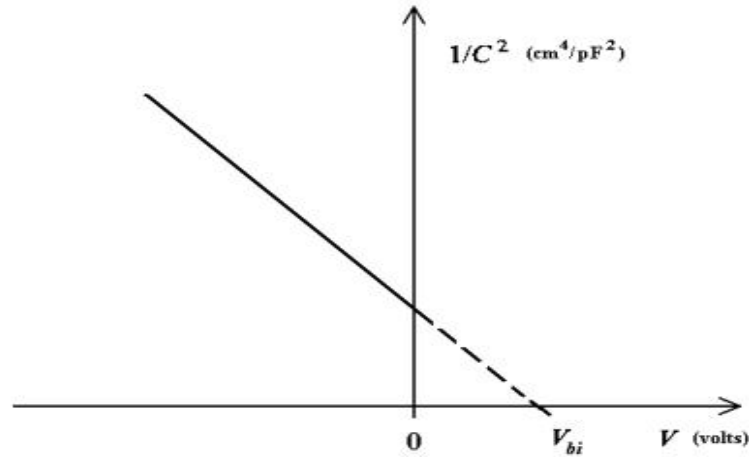


Fig31 $1/C^2$ plot of the barrier capacitance used to determine the background concentration N_B and built-in potential V_{bi} of a semiconductor junction [32]

3.4.3 Structural Analysis

3.4.3.1 TEM Characterization

Transmission electron microscopy (TEM) is an analytical tool allowing visualization and analysis of specimens that can reach realm of (1 nanometer (nm) = 10^{-9}m) [33]. With TEM, crystal structures, specimen orientations and chemical compositions of phases, precipitates and contaminants data can be enabled through diffraction pattern, X-ray and electron-energy analysis (Fig.32) [33]. TEM is a microscopy technique modeled with three steps; firstly, a beam of electrons is transmitted through an ultra-thin specimen, secondly; interacting with the specimen as it passes through and finally, structural image formation from the interaction of the electrons transmitted through the sample. Typically, the image is magnified and focused onto an imaging device by either ways, whether on fluorescent screen or to be detected by a sensor such as a CCD camera [34].

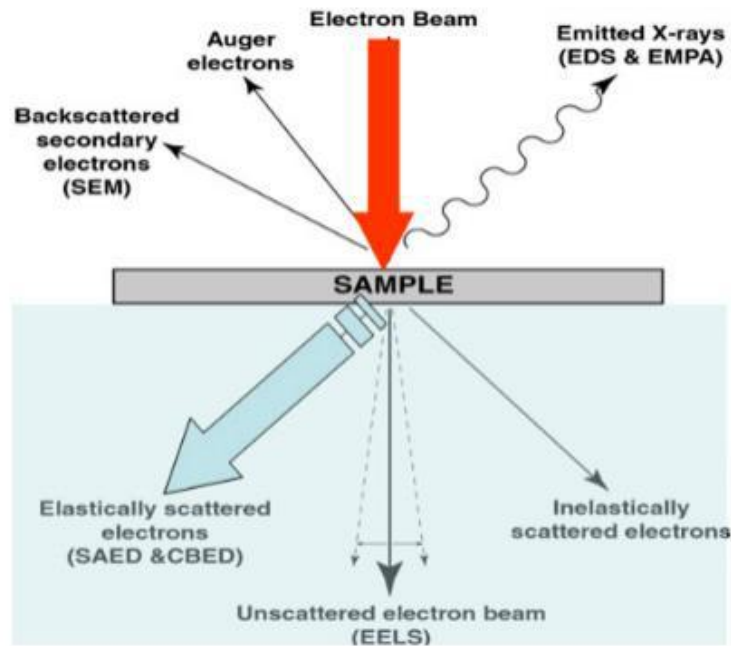


Fig.32 Various electron beam sample's interaction. TEM exploited various transmitted electron interaction with sample [33]

In TEM, several useful modes are available, however the main famous mode is TEM mode which uses a broad stationary electron beam on the sample where correlation exists between the object and the image plane, (like with an optical microscope). Diffraction effects in the real space is results of crystal lattice orientation along with material density variations gives rise to image contrast. At high magnification and for very thin foils interference of transmitted and diffracted electrons gives rise to phase contrast used for High Resolution TEM (HRTEM)[34].

The second important mode is STEM (Scanning Transmission Electron Microscopy) mode uses a fine focused beam which is rastered over the sample. In STEM mode the intensity of the scattered (or un-scattered) electrons is detected synchronously with the rastering of the beam and used to generate a 2D image. Usually the large angle scattered electrons are used which is called High Angle Annular Dark Field STEM (HAADF-STEM) where the brightness is in first approximation proportional to the square mean value of the atomic number and is therefore strongly composition dependent. . While, diffraction effects are weak in HAADF-STEM mode, images can also be acquired with low angle ("Annular Bright Field, ABF-STEM) which displays lighter materials image or medium angle (Dark Field, DF-STEM) scattered electrons. In these cases, diffraction effects are important and lattice defects will show up more clearly, thus this mode is useful for sample defects analysis [35].

4. Chapter Four: Results and discussion

4. Chapter Four: Results and discussion

In this chapter, the following experiments were carried out in to investigate the evolution of sputtered MoO_x process condition (i.e. deposition power, oxygen flow rate and argon flow rate) and post annealing process followed by characterization measurements of the experiment's samples. Finally, this chapter is concluded with portraying bottlenecks which may hinder the successful operation of sputtered MoO_x hole selective contact for silicon heterojunction solar cell .

Following the wafer cleaning process, deposition condition study were carried out to find the suitable conditions that give rise to near stoichiometric MoO_x. Once the near stoichiometric MoO_x initial process conditions (range) is found out through initial established indicator tests (hysteresis analysis), Elastic Recoiling Detecation Analysis (ERDA) measurements were conducted to find out suitable, stable and reproducible sputtering conditions. The successive measurement of X-ray Photoemission Spectroscopy (XPS), Photoluminescence (PL) and Transmission Electron Measurement (TEM) on the wafer's scale samples were carried out to investigate photovoltaic properties made of sputtered MoO_x hole selective contact.

4.1 Deposition conditions study

In this section, right after wafer cleaning process with short dip in diluted hydrofluoric Acid (HF~.01%), wafer samples were loaded in Nimbus 310 RF-sputtering tool. Since, global process conditions (plasma power, argon flow and oxygen flow) reported in table.2 section 3.2 has to be controlled and would give rise to the optimized near stoichiometric of MoO_x (i.e. oxygen to molybdenum ratio is round 3 to 1), the experiments strategy is to narrow down such parameters dynamic range. Firstly, with varied plasma power and oxygen flow and fixing argon flow. This can be justified based on the previous sputtering reports where plasma power and oxygen flow variation yielded stoichiometric MoO₃ ratio [15]. Third controlling parameter i.e. Argon flow variation effect on the stoichiometry ratio is consequently investigated for obtaining the optimum solar cell performance results.

4.1.1 Plasma power study

Starting decently from high power range (5000 W, 4000 W, 3000 W,2000 W and1000 W) and seeking for research target i.e near stoichiometric ratio of MoO_x ($x\sim 3$), deposition rate

dependency studies were conducted on early experimental stage so as to provide trendline for chemical compound composition control [15].

Fig.33 shows dependency relationship between deposition rate and deposition power at fixed oxygen flow at 20sccm and argon gas flow at 200sccm . Obviously, functional dependence of deposition rate on deposition power is by large follows proportional increment behavior, which is attributed to the of increase sputtering of Argon ions current increase as result of deposition power increase i.e. more argon ions generated, which in turn increase sputtering yield of the compound reacted material. However, there is noticeable jump from 1000 W to 2000W and from 4000W to 5000W as well, which can be speculated as two critical jumps in MoO_x composition related to compound materials interesting composition for given oxygen and argon flow (i.e. extremely insulating to metallic film characteristic). The product of this study is tuning MoO_x layer thickness. Luis et al. [11] showed how critical thickness may impact cell efficiency and incident photocurrent density [11], however, MoO_x layer with lower thickness between 6-10nm is implemented presuming to enhance light transmittance window and carrier transport as proved by [11].

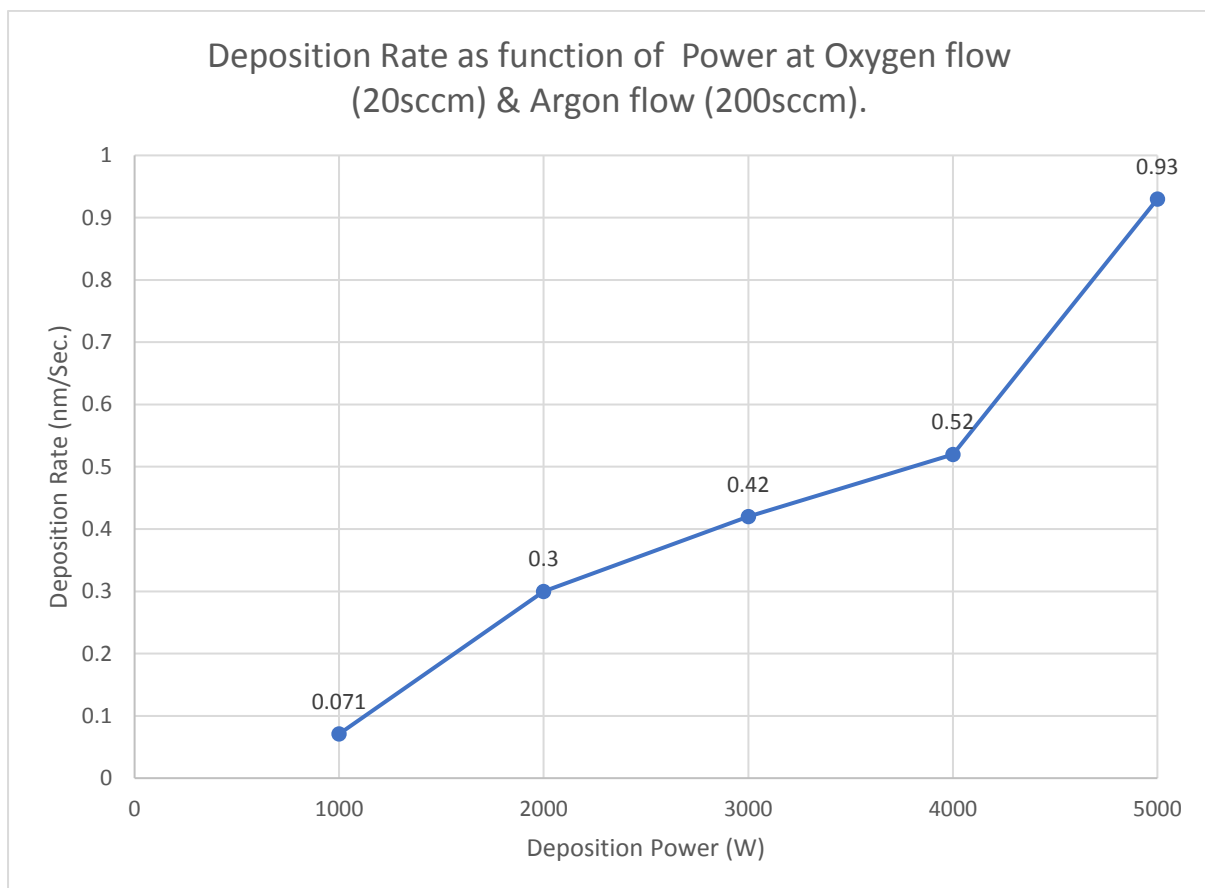


Fig.33 Deposition rate of MoO_x layer as function of deposition power for oxygen flow (20sccm) and argon flow 200sccm

A second study of deposition power is deposition rate functional dependence on oxygen partial flow (O_{PF}) which is defined as:

$$O_{PF}(\%) = \frac{O_{2,F}}{O_{2,F} + Ar_F} \quad \text{EQ.14}$$

Where O_{2,F} and Ar_F are the oxygen and argon gas flow in sccm.

By fixing deposition power of 1000 W, 2000W, 3000W, 4000W and 5000W then varying oxygen flow from 20sccm to the maximum allowable oxygen flow (100sccm), Fig.34 (a-e) can be read in conjunction with Fig.35. Fig. 34 (a-e) portray hysteresis analysis examples for high deposition power 5000W, 4000W and 3000W and lower deposition power 2000W and 1000W respectively. With increasing and decreasing sequence of Oxygen flow and recording corresponding oxygen partial pressure which is defined as:

$$O_{2,PP} = (P_{total} - Ar_p) \quad \text{EQ.15}$$

Where O_{2,PP} denotes oxygen partial pressure, P_{total} is total recorded pressure at given power and given Argon flow and Ar_p argon gas partial pressure measured at no oxygen flow (i.e. pure Mo sputtering). Interestingly, Oxygen partial pressure O_{2,PP} = (P_{total} - Ar_p) as function of Oxygen flow for (a)5000W, (b) 4000W, (c)3000W (d)2000W and (e) 1000W deposition power at O₂ flow (200sccm) and Ar. Flow (100sccm) which shows nonlinear relationship at 5000W power condition and almost neglected hysteresis. At 4000W, 3000W, and 2000W nonlinear relationship with considerable hysteresis width decreasing towards 2000W. A hysteresis width is approximately ~ 0 sccm for 1000W and almost sub-linear functional dependency.

Fig.35 demonstrates decreasing trend as oxygen partial flow increased for all power range investigated (i.e. 5000W,4000W,3000W,2000W and 1000W). In general, we notice deposition rate is high which mostly implies metallic formation at low oxygen partial flow, however, convergence is observed at higher oxygen partial flow. This has been explained by Berg model [15] mainly as results of target oxygen poisoning. Berg [15] proved that the sputtering yield of the compound material is substantially lower than the sputtering yield of the elemental target material which in turn causes the deposition rate to decrease as the supply of the reactive gas increases [15]. As with behavior of 1000W curve in Fig.34 which showed lower and sublinear hysteresis behavior, remarkably, again it showed in Fig.35, at 1000 W much less steep slope variation is noticed in comparison with higher deposition power. This trend might be explained by perception that at low power there is higher

probability of finding targeted oxygen to molybdenum ratio (i.e. O/Mo ratio is around 3 to 1) as result of overwhelming target and substrate poisoning. Moreover, it is believed that there is contribution of sputtering by oxygen ion which explain the less sputtering at higher oxygen flow rate for the fixed argon ion generation rate.

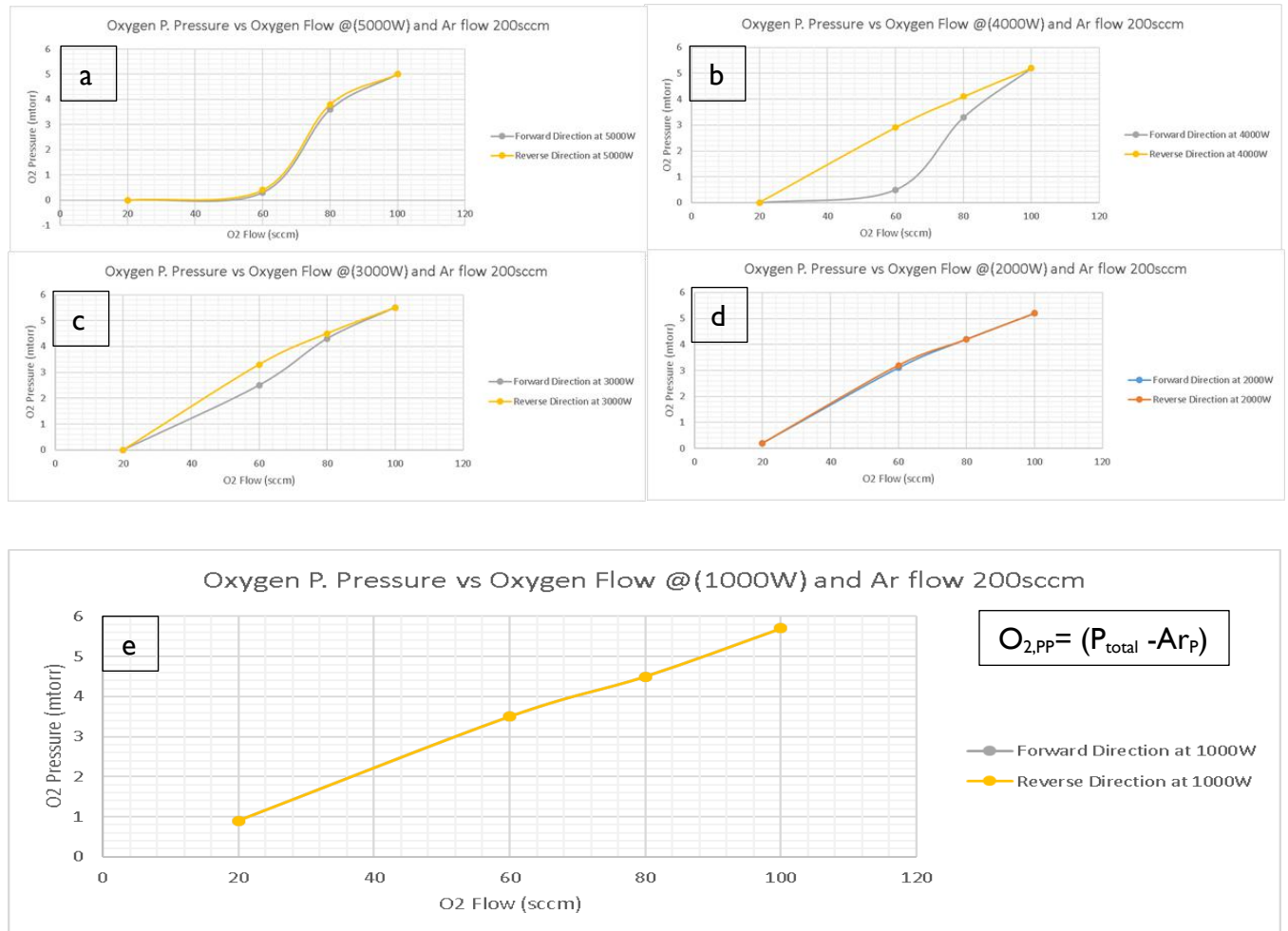


Fig.34 Oxygen partial pressure $O_{2,PP} = (P_{total} - Ar \cdot P)$ as function deposition of Oxygen flow for (a)5000W, (b) 4000W, (c)3000W (d)2000W and (e) 1000W deposition power at O_2 flow (200sccm) and Ar. Flow (100sccm) which shows nonlinear relationship transition at 5000W power condition and almost neglected hysteresis. At 4000W, 2000W, and 2000W nonlinear relationship with considerable hysteresis width decreasing towards 2000W . A hysteresis width is approximately ~ 0 sccm for 1000W and almost linear functional dependency.

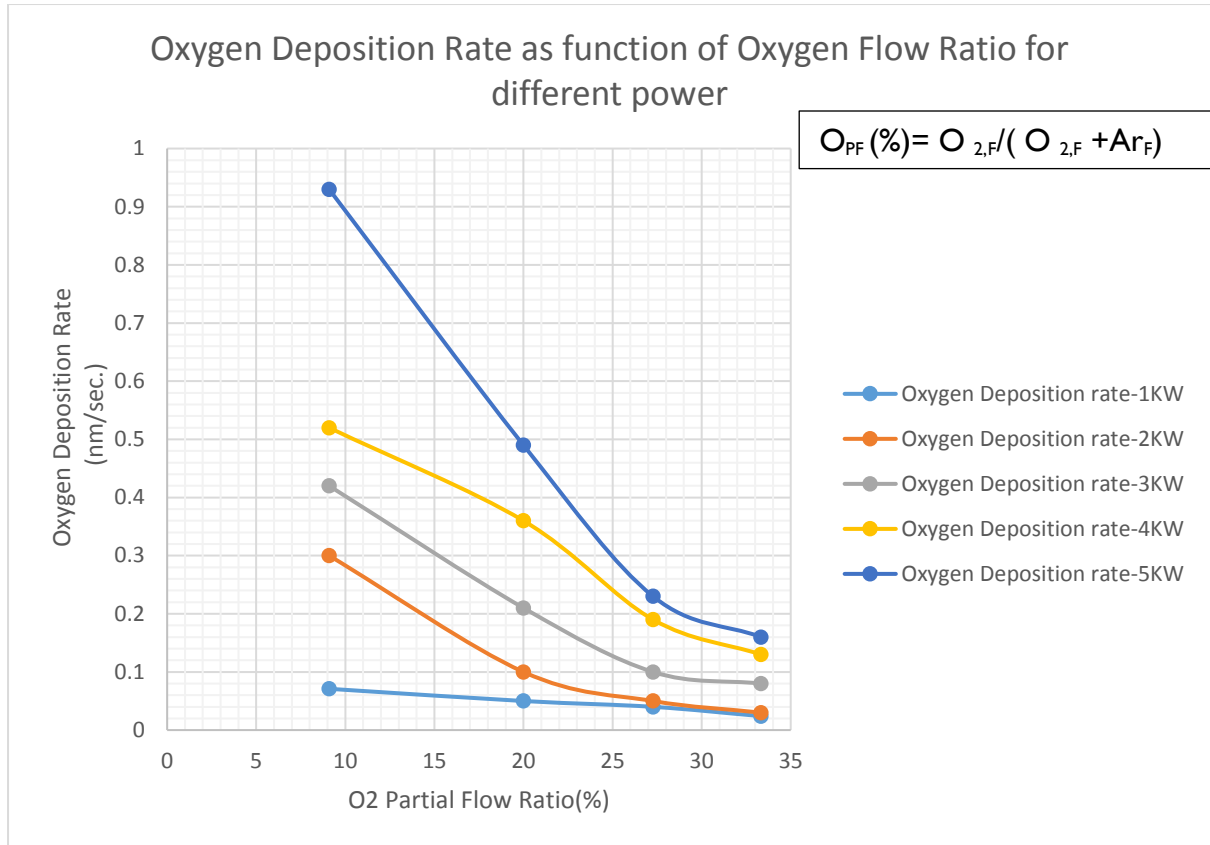


Fig.35 Deposition rate as function of partial Oxygen flow ($O_{PF} (\%) = \frac{O_{2,F}}{O_{2,F} + Ar_F}$) for 1000W and 2000W deposition power.

4.2 ERDA Analysis for O/Mo ratio

Based on previous power study analysis and film resistivity analysis, samples have been elected for ERDA analysis. ERDA results in Fig.36 is revealed for 1000W and 2000W based on the pervious subchapter analysis, as result, in Fig.36 higher but not satisfactory O/Mo ratio were obtained. It is noteworthy to mention that as for low power 1000W and 2000W, the best oxygen to molybdenum ratio obtained is 2.46 and 2.3 consecutively obtained at higher oxygen flow rate ($O_2 = 100\text{sccm}$). So going for below 1000W will -to great extend- yield stoichiometric composition. One piacular result for 1000W at oxygen partial flow ($O_{2,PF} = 20\%$) having slightly less O/Mo ratio in comparison with 2000W for the same oxygen parital flow value with no clear clue whether it is characterization tool influence or real noise O/Mo ratio in the sample presented for measurement.

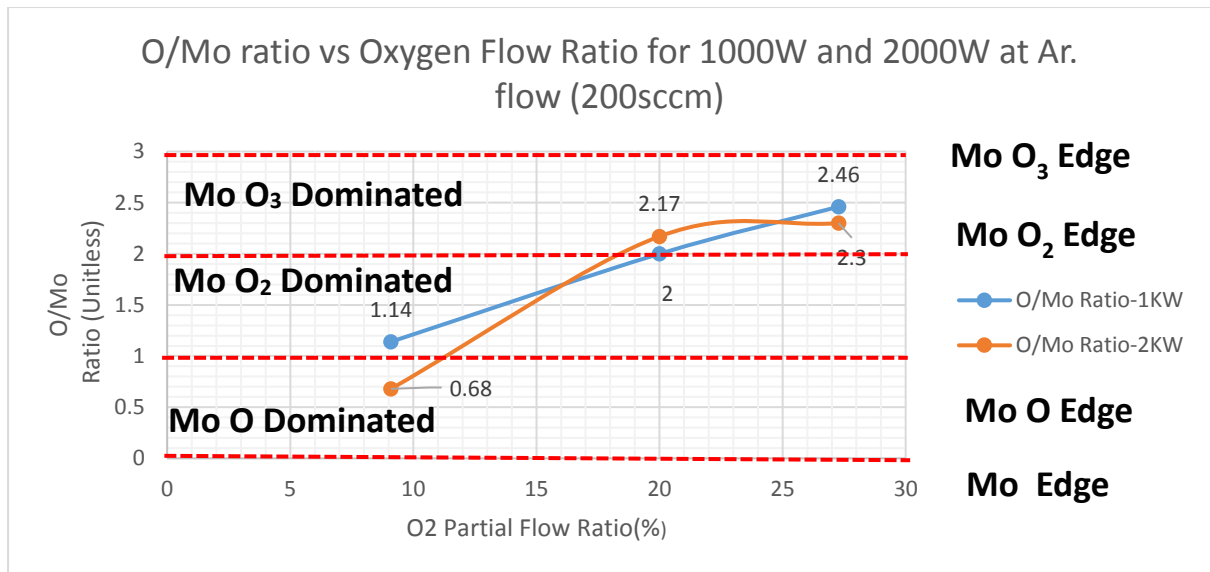


Fig.36 O/Mo ratio atomic ratio measured with ERDA as function of Oxygen partial flow i.e. $O_{PF}(\%) = \frac{O_{2,F}}{O_{2,F} + Ar_F}$, 1000 and 2000W respectively with each composition edge denotes the end of one composition state and beginning of the next one.

For having an idea about argon gas flow influence (sccm) on film composition, Fig. 37 shows the influence is clear at range from 50% to 100% of argon flow ($Ar = (100 \text{ to } 125) \text{ sccm}$). In particular, the only explanation we owe is that, as assumed by Berg model for sputtering of target which took place with low argon ion which indicates a contribution of sputtering by ionized reactive gas (O_2). However, this contribution is neglected in the original Berg model and reasonably is neglected at lower reactive gas partial pressure [15].

One important point to note is appearance of hydrogen and carbon (Fig.38) significantly with low power conditions with hypothesis for this notable presence; it could be natural for lower power conditions which promote lower temperature conditions and favors the presence hydrogen and carbon molecules in the chamber. An other hypothesis is related to lower chamber bases pressure. In reality and during deposition, sputtering tool experienced multiple errors and breakdowns concerning base pressure, hence we had to go with next step of the acceptable lower base pressure which might promote deposition of organic elements in the chamber on the substrate. Furthermore, the presence of inorganic Aluminum (Al) in one set of samples with lower base pressure conditions had already detected.

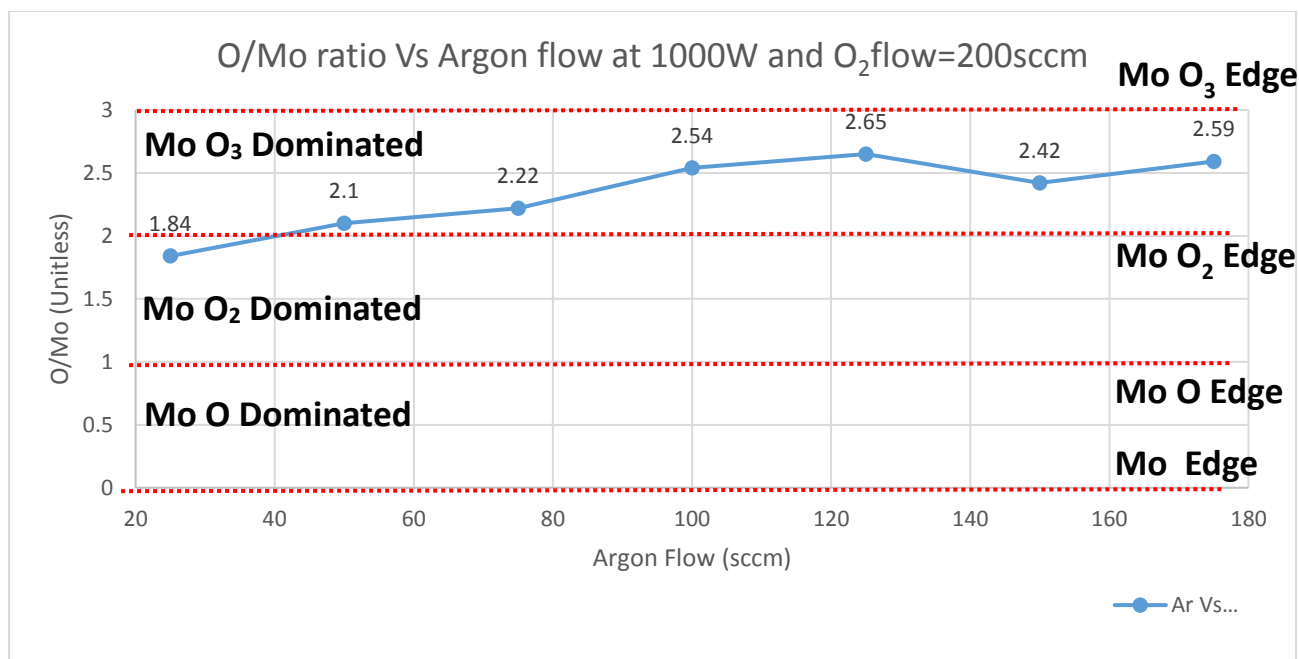


Fig.37 O/Mo ratio atomic ratio measured with ERD as function of Argon flow rate at power of 1000W with each composition edge denotes the end of one composition state and beginning of the next one.

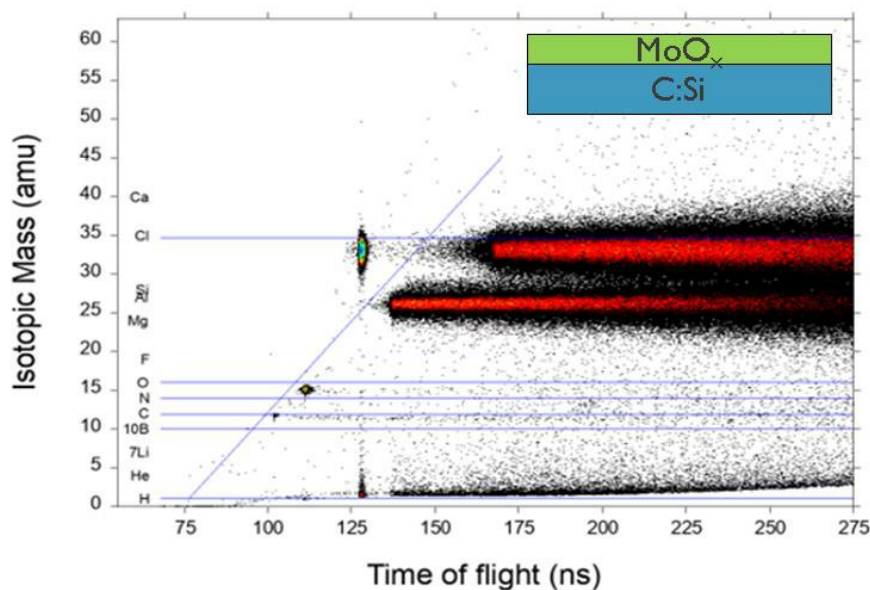


Fig.38 O/Mo ERDA isotopic mass of all typical elements that might be in the test sample for different flight times, we can notice Al presence in Si sample and traces of carbon and hydrogen in 1000W, Traces of Al can be noticed due to cross contamination occurrences. Inset shows sample structure for ERDA measurement.

4.4 XPS Measurement Results

Obviously, from all previous results of high sputtering power, the highest O/Mo ratio obtained is 2.65 at full oxygen flow rate scale (100 sccm) and almost 50% of full argon flow scale (200sccm). Then we became certain that near stoichiometric range of sputtering conditions

is below 1000, with XPS we confirmed the ERDA results of 50W, 100W & 600W. (O/Mo ~2.9). While previous samples in (section 4.3) represent as deposited condition, different post deposition conditions are referred in Table.3. In Table.3 showed samples with as deposited 50W, (three samples) with 100W deposition power (with no annealing, with post annealing for 60min at 160 °C and same sample with ITO capping) and one sample with 600W (annealed for 60 min. at 160 °C) has near or stoichiometric atomic composition of MoO_x.

Accordingly, in Fig.39(a) two integrated doublets (for all samples except 50W sample) are observed centered at Mo_{3d 3/2}~236.5 eV and Mo_{3d 5/2}233 eV respectively. In that regard, each doublet contains to oxidation states Mo⁺⁶ and Mo⁺⁵ (not shown in the Fig.39) and doubles approximate shape look similar to the ones obtained with evaporated MoO_x in Fig.39(b) [11,16]. This remarkably, confirm our previous results (power deposition and ERDA results) obtained with highest oxygen partial flow at 100% (100sccm).

With regard to the calculated work function with the calculation of the WF was performed using the methods in Ref. [36], after measuring the Fermi edge on a silver sample, the highest desirable work function obtained is too low than the reference vwork function value i.e. 6.08eV at 100W power in comparison with reference value 6.7eV [11].

Table .3

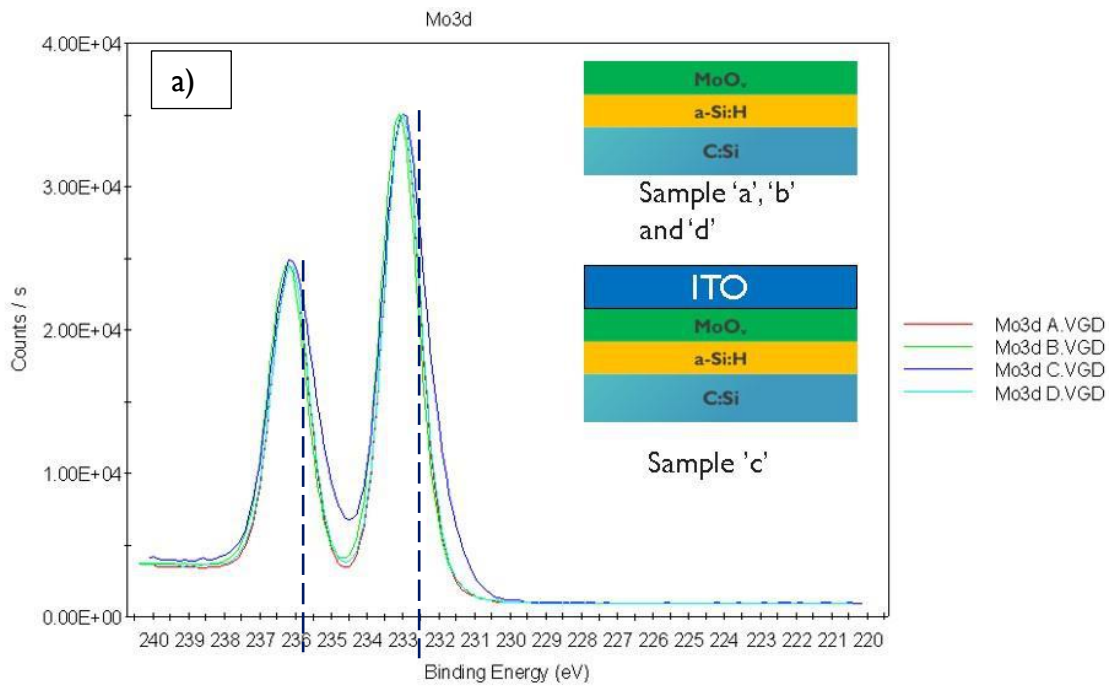
Chemical composition analysis result measured by XPS for MoO_x

Sample	(O/Mo) Ratio	Work Function (eV)	Remarks
50W-Not annealed	4.00	5.5	SiO _x is higher than 100W
100W- Not annealed	3.00	6.08	no traced MoO ₂ concentration
100W- Annealed for (60min @160°C)	3.03	4.99	no traced MoO ₂ concentration
100W- Annealed for (60min @160°C) with ITO		4.79	MoO ₂ (1.99) concentration
600W- Annealed for (60min @160°C)	2.91	5.55	no traced MoO ₂ concentration

Furthermore, work function for as deposited 100W sample was 6.08 eV which is higher than the annealed one i.e. 4.99 which is could be attributed to development of crystalline phase. However, Neusel et al. [17] and although, their annealing condition were in different gas atmosphere (i.e. H₂, Ar, O₂, CO₂) while our sample is annealed in N₂ atmosphere, they concluded with the need for engineering for effective work function to encounter high work

function lowering challenge which is responsible for the induced bend bending needed for better bulk carrier inversion.

So far we can say the best condition yielded the best O/Mo ratio and work function is sample deposited with 100W, O₂ flow of 100sccm, Argon flow is 100sccm and annealed at 160°C for 60 minutes. Further discussion on the work function in C-V measurement section.



39

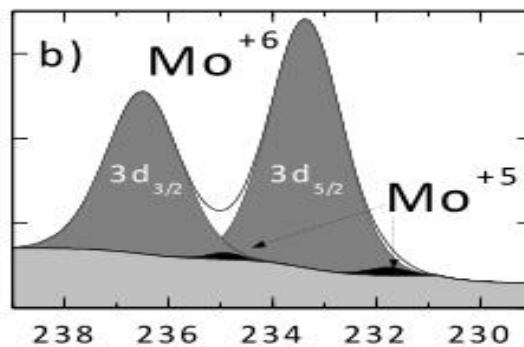


Fig.39(a) Overlay Mo3d of samples ('A' '100W- not annealed', 'B' 100W annealed for 60min', 'C' 100W annealed for 60min and with ITO and 'D' 600W annealed for 60min), presented in angle integrated mode- graphs are auto-scaled to enable chemical comparison, MoO₃ was detected on all sample, on sample 'c' (capped with ITO) also a doublet at lower binding energy (blue color) was detected due to presence of metallic compound in the sample.(b) XPS spectra of the core levels of MoO_x from reference [11].

4.5 Passivation study Result

Concerning basic passivation measurement mentioned in section 3.4.2.2 and 3.4.2.3, passivation quality test with PL measurement and SunsVoc measurements were conducted.

PL images in Fig.40 show all deposition and post deposition states for 100W sample. In Fig.40 (a) fresh sample of PECVD deposited a-Si:H(i) on the front side of textured mirror polished surface of c-Si and n-aSi:H on the rear side of the wafer were measured and yielded considerable excellent passivation PL value (i.e. more much brighter). In contrast to that, in Fig.40(b) the measurement were taken right after RF-sputtering process and deposition of MoO₃ which shows absolutely high sputtering damage inherited in the sample and thus all area is in dark color (poor carrier lifetime). Slight enhancement to the as deposited sample is observed in Fig.40 (c) after post annealing temperature 160 °C for 30 minutes in nitrogen atmosphere. Adding more annealing time for the similar previous temperature in Fig.40(d) for 1 hour caused sample to look more brighter in PL which is an indication of considerable carrier lifetime improvement due to more annealing time. Such increase in annealing time might be attributed to the induced development of crystalline phase change (if any) from amorphous phase to more conductive phase. However, more XRD investigation is required for confirmation of such crystallization. Moreover, in terms of implied V_{oc}, it is fitted and calculated from QSSPC (i.e. EQ.9) results to give value of 719mV for the last sample case i.e. Fig.40(d). Important point to note is that, QSSPC were not extractable for Fig. 40 (b) and very low in case of Fig.40 (c). In general the lifetime value order of Fig.40 (d) is on micro-second at effective carrier density of 1E+15.

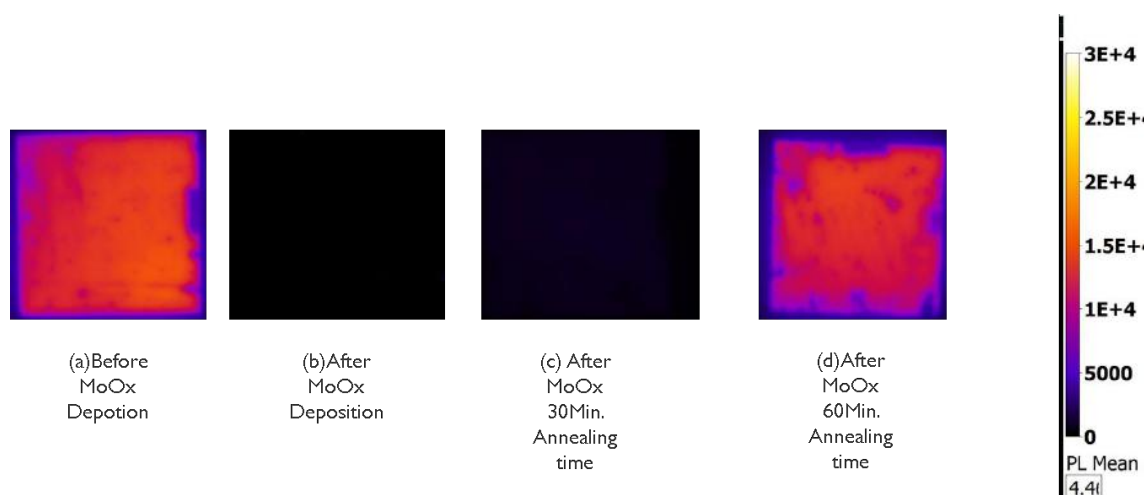


Fig.40 PL imaging for various samples (a) before MoO_x deposition, (b) as deposited MoO_x, (c) sample annealed at 160 °C for 30min and finally (d) sample is annealed for 1 hour with noticeable improvement in bright color scale.

By measuring SunsVoc for the Fig.40 (d) (with ITO and silver on both sides of the wafer) at the best conditions so far (power (100W), Argon flow (100sccm) and O₂ flow (100sccm) and annealed at 160 °C for 60min, result yielded cell Pseudo-efficiency 14.9% at open circuit voltage value at 465mV as shown in Table.4, which is considerably low in comparison with reported value 600mV Fig.41 [3]. Using the figure of merit reported by Bivour et al. in [3], the high loss in selectivity is denoted by $\Delta V=254\text{mV}$, Table.5.

Table .4 Extracted typical cell parameters values for sample deposited at conditions (power (100W), Ar flow (100sccm) and O₂ flow (100sccm) and annealed at 160 °C for 60min

Voc (V)	Vmp (V)	Jmp (A/cm ²)	PFF	Pseudo Efficiency	Apparent Rs (Ω-cm ²)	Ideality (n) @ 1 sun	Ideality (n) @ 0.1 sun	Voc @ 0.1 sun	Jo1 (A/cm ²)	Jo2 (A/cm ²)	Fitted Rsh (Ω-cm ²)
0.465	0.426	0.035	0.891	14.9	0.25	0.33	0.46	0.441	5.4E-10	1.0E-11	150000

Table .5 calculated iVoc, measured SunsVoc, and selectivity measurement ΔV .

Fitted iVoc (mv)	External SunsVoc(mV)	ΔV (mV)	Potential Loss(%)
719.0	465	254.0	35.3

Fitted iVoc (mv)	External SunVoc(mV)	ΔV	Potential Loss(%)
719.0	465	254.0	35.3

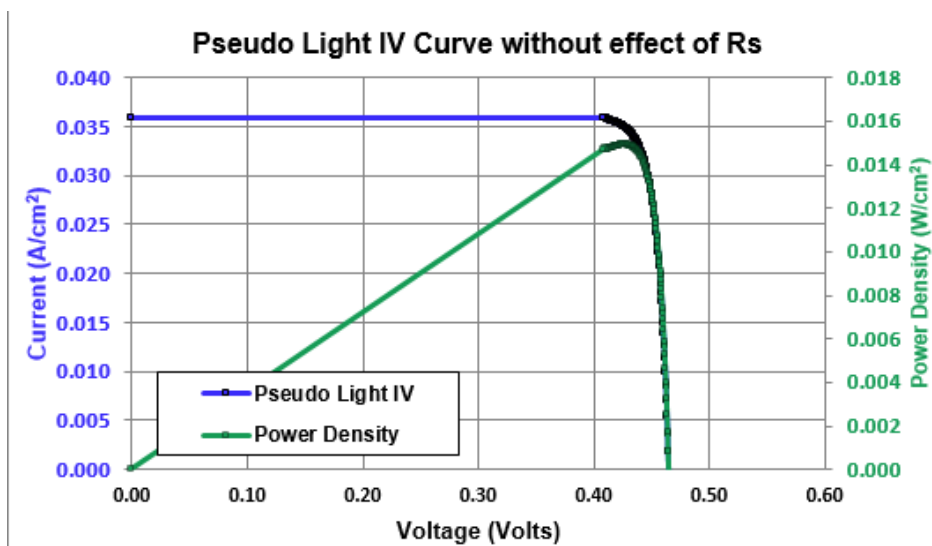


Fig.41. Pseud IV curve for sample at conditions (power (100W), Ar flow (100sccm) and O₂ flow (100sccm)

4.6 Band bending study with C-V Measurement

Last electrical measurement test were conducted to obtain band bending is C-V study. However, we have used the same structure of the pervious study with the exception of (using

flat surface mirror polished wafer and local front ITO and silver contact) for C-V measurement. The flat band voltage result for sample deposited at conditions (power of 100W, Ar flow of 100sccm and O₂ flow of 100sccm) and annealed at 160 °C for 60min has the highest flat band voltage which is 457.3mV in Fig. 42. This result dictate more research for low work function dependencies reported by Greiner et al. [13] and whether other factors like film preparation methods has dominant effect as much high as stoichiometry. From MOS model It is well known that flat band voltage value depends on work function difference of interface materials, surface dipole, developed oxide fixed charges . At this moment, we may attribute low flat band voltage to the low work function obtained (after annealing process) with sputtered MoO_x results (refer to Table .3). However, interface dipole, developed oxide fixed layer charges require separated and distinctive study (i.e. out of scope of this research work).

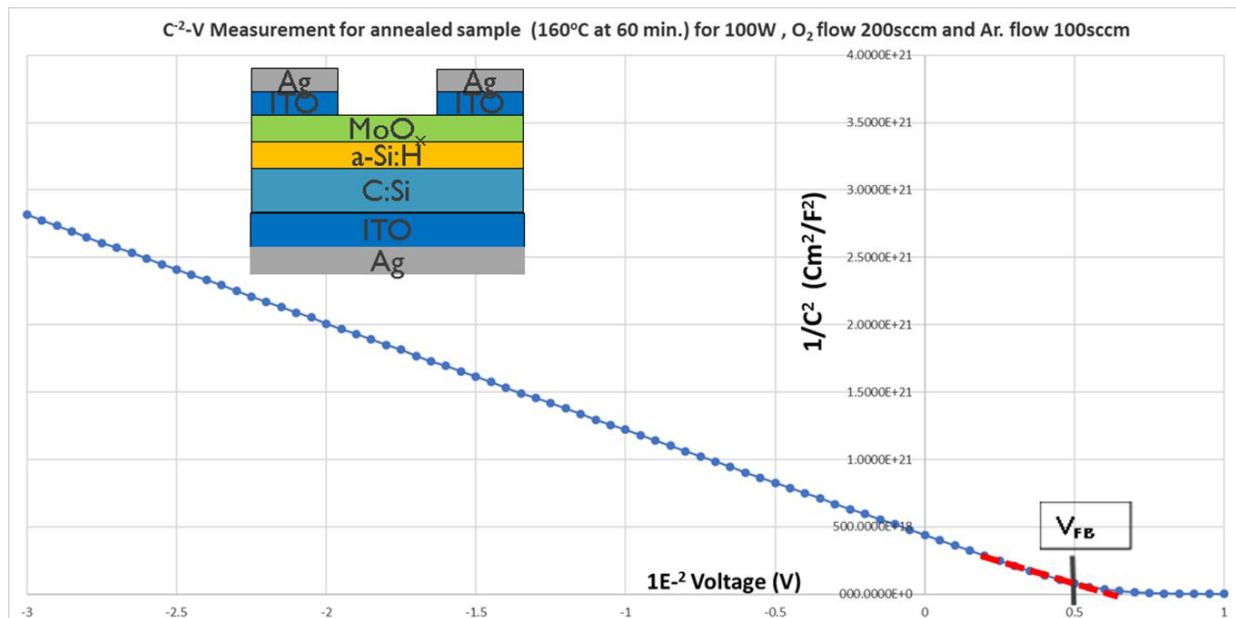


Fig.42 $1/C^2$ vs voltage profile for sample deposited at conditions (power (100W), Ar flow (100sccm) and O₂ flow (100sccm) and annealed at 160 °C for 60min where black line is $1/C^2$ trendline and green dashed line extrapolating calculated $1/C^2$ is used for extracting flat band voltage value.

Fig.43. shows the results of power 100W, Argon flow (200sccm) and O₂ flow (100sccm) for different annealing conditions. During sputtering, negative ions or Argon ions induced oxygen vacancy or incorporation of other elements could be reason for low work function. During annealing process, we may come with loss of oxygen (i.e. oxygen defects) during annealing as possible reasons which may promote better carrier transport conduction and low work

function. Although, work function were reduced after annealing, interestingly, the best results of flat band voltage obtained with annealing for 60 minutes at 160°C which may indicate stress relaxation, passivation recovery or change in grain size.

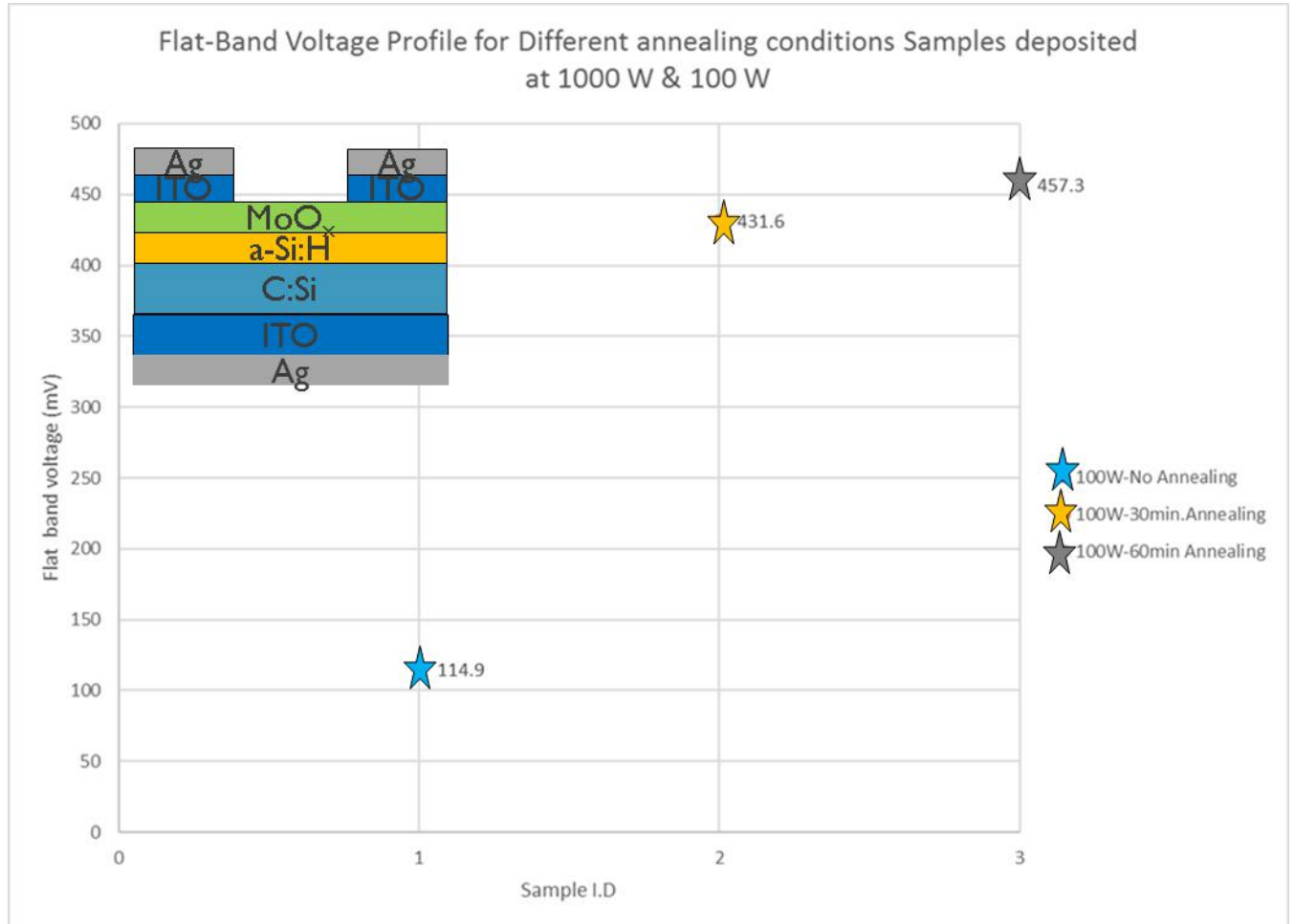


Fig.43 Flat band voltage for sample with deposited at conditions (power (100W), Ar flow (100sccm) and O₂ flow (100sccm) and not annealed (sample A), annealed at 160 °C for 0min (sample B) and annealed at 160 °C for 60min (sample C), inset shows typical sample structure .

4.7 TEM Characterization Results

As far as concern sample sputtered with 100W deposition power, O₂ flow (200sccm) and Ar. Flow (100sccm) conditions and annealed at 160°C for 1 hour time, TEM characterization on random pyramids textured wafer with all possible high resolution modes along with compositional analysis modes were measured in IMEC facilities[37].

Out of different high resolution modes, ABF-STEM in Fig.44 (a) and Fig.44 (b) for EDS measurement, the clearest sample layers for cross sectional determination for (light elements layers visualization) and composition determination were obtained. Fig.44 (a) reflects similar

half sectional layers referenced in Fig.45 in interfacial layer between ITO and MoO_x . Yet couple of very thin interfacial mixed layers presented in Fig.44 (a and b). The first interfacial layer is interfacial layer is between ITO and MoO_x and the second one is SiO_x between MoO_x and a-Si:H(i). While the latter might be developed during sample transfer and/or during plasma deposition, the first is already been highlighted by Jonas et al. [14] in their experimental work in Fig. 45. They suggested that the MoO_x /TCO interlayer (i.e. indicated with an arrow) which getting thicker with annealing has resulted in dramatic deterioration of the performances of their MoO_x -based cell which resembles hole-blocking barrier[14]. However, in their experiment, MoO_x is deposited with evaporation technique and in our case, sputtered MoO_x were employed. We may speculate another possible reason for the development of this mixed oxide SiO_x layer between MoO_x and a-Si:H before annealing. Sputtered MoO_x on top of a-Si:H might initiated reaction product of defected mixed layer which might be thicken with annealing temperature process and hence resulted in lower work function reported in passivation study (section4.5).

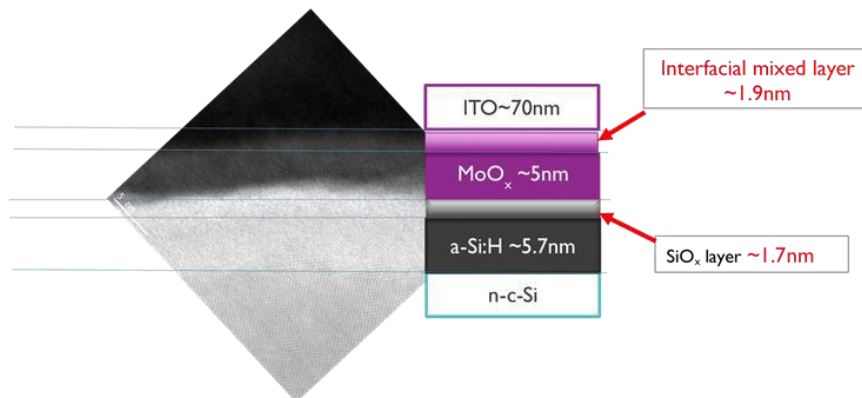


Fig.44 (a) ABF-STEM cross section for 100W sample, which highlight each layer along with interfacial layer.

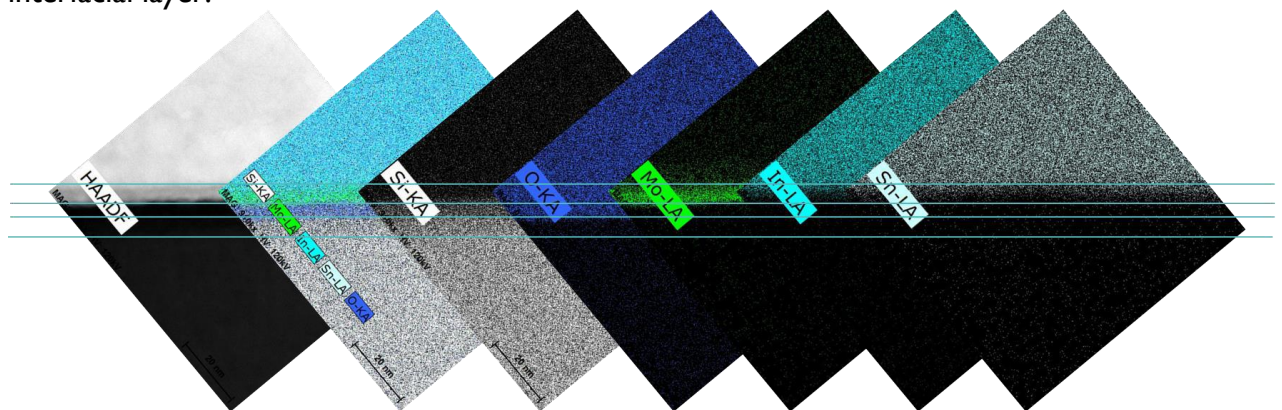


Fig.44 (b) EDS measurement cross section details for Fig.45(a) with each chemical element showed with specific color.

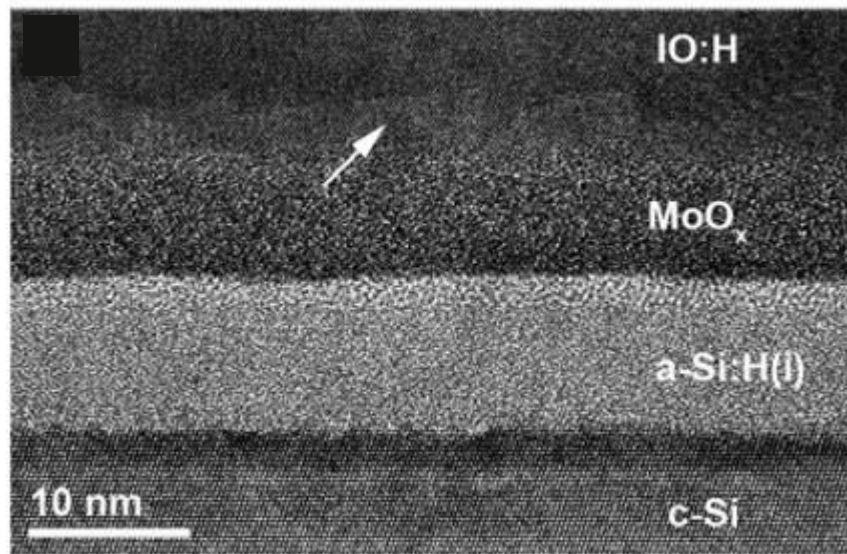


Fig.45 by Geissbühler et al. for HR-TEM micrographs of the c-Si/a-Si:H(i)/MoO_x/IO:H interfaces after annealing at 200 ° C in N₂ for 25min. Images are purposely defocused to increase the contrast of the MoO_x/IO:H interfacial layer[14].

Finally, EDS raw data analysis in Fig. 46 reflects the similar layers ordering in Fig.44(b) but with spatial atomic distribution details showing each element depth distribution. EDS raw data analysis suggests that development of interfacial layers indicated with no sharp elements slope, rather less steeper slopes are shown in Fig.46. The profiles of the In and the Mo also overlap, less than those of Mo and Sn, indicating maybe some diffusion of In into the MoO_x which can be roughly evaluated with slope of each element.

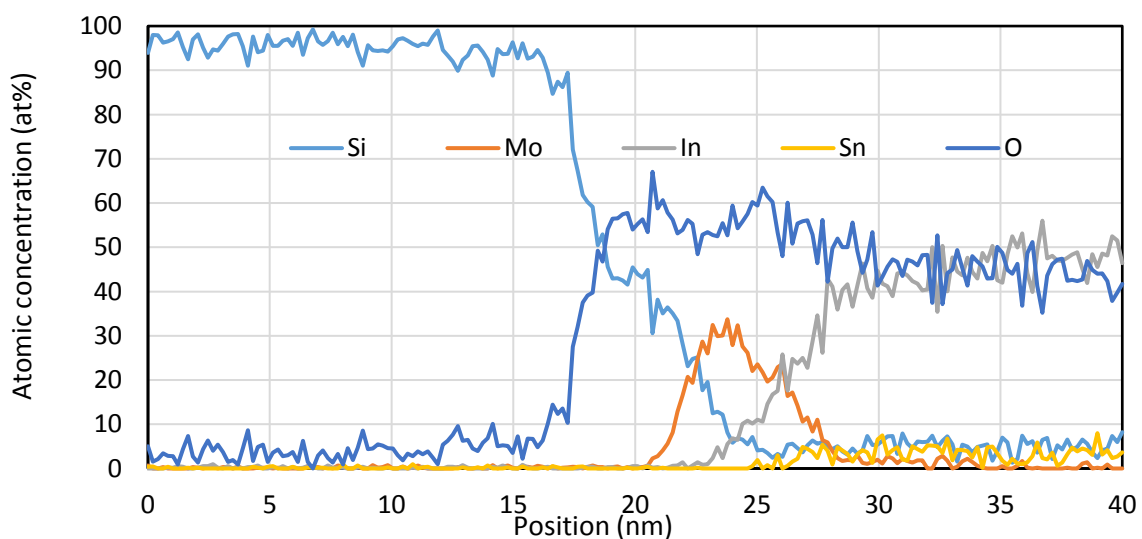


Fig.46 Illustrate reconstruction of atomic concentration spatial distribution from EDS raw data measurement.

However, since TEM is mainly intended for accurate structural analysis not for accurate compositional analysis, below 10% atomic concentration distribution in Fig.46 is not accurate to assess precise sample composition, hence the values close zero is considered as low signal to noise ratio i.e. background disturbance.

4.8 Qualitative loss analysis for low performance of sputtered MoO₃:

Loss analysis systematic study has to consider two separate route; Voc study and V_{FB} study. With regard to the first factor, it is imperative that, one of the most important parameter that substantially determine the operational performance of solar cell is open circuit voltage (V_{oc}). The reported V_{oc} which is 465mV depends upon various factors depicted in Fig. 47 by Elumalai et. al. Although it was reported for Organic Solar Cells (OSCs), similar analysis approach could be valid for our silicon heterojunction solar cell enabled with MoO_x hole selective contact [38].



Fig. 47 Factors influencing the open circuit voltage (V_{OC}) in organic solar cells. Each parameter influences the V_{OC} either directly or indirectly via interrelated dependencies among them. Inner circles presents direct or most influencing factors while the outer ones manifest indirect and less significant factors dependent V_{oc} [38].

Interestingly, our calculated implied V_{oc} yielded higher value roughly around 719 mV with loss in selectivity ΔV is equal to 254 mV. This huge loss in the classic sense with recombination current is not enough for mathematically assess V_{oc} according to EQ. 16. Rather, as reported qualitatively by Bivour (for MoO_x) [3] and rigorously by Mikolášek (for SHJ) [39], EQ.17 represents modification on V_{oc} formula with indirect an inclusion of band bending (carrier inversion at c-Si interface) EQ.17 and Fig.48. Defected and developed interfacial oxide layers between sputtered MoO_x and a-Si:H requires more details compositional and conditional investigation study. Moreover, Developed defective interfacial layers (i.e. the a-Si:H- MoO_x and MoO_x -ITO interface) along with oxygen vacancy defects and other impurity defects distribution in the MoO_x band gap is required to evaluate the dominant factors for low V_{oc} (i.e. band bending, surface recombination or both)

$$V_{OC} = \frac{E_{g-Si} - \delta_{Si(n)}}{q} - \frac{kT}{q} \ln \left(\frac{N_V}{\Delta p} \cdot \frac{\frac{D_n + S_n}{L_n}}{\frac{D_p}{L_p}} \right)$$

EQ.16

Where T is the temperature, q is the elementary charge, k is the Boltzmann constant, E_{g-Si} is the band gap of c-Si, N_C and N_V are the effective densities of states in the conduction band of c-Si, $\delta_{Si(p)}$ and $\delta_{Si(n)}$ are the dopant activation energies of c-Si substrate with p-type and n-type doping, respectively, L_p and L_n are diffusion lengths for holes and electrons, respectively, and D_p and D_n are diffusion constants for holes and electrons. Further symbols denote the interface recombination velocities for holes $S_p = C_p D_{it}$ and electrons $S_n = C_n D_{it}$ where C_p and C_n are the capture rate coefficients for holes and electrons, respectively, and D_{it} is the interface defect density. The Δp and Δn in the equations denotes the excess carrier concentration [39].

$$V_{OC} = \frac{\Phi_B}{q} - \frac{AkT}{q} \ln \left(\frac{qN_V S_p}{j_{sc}} \right)$$

EQ.17

itself is believed in the photocatalytic application film preparation to be source of shallow oxygen vacancies donors nears conduction band which in turn lower the work function parameter [42]. Another possible source for work function lowering is reported by Kang et al. [43] indicates that plasma damage due to long deposition time is source for work function lowering in TaN-gated MOS [43]. Another interesting source for work function lowering is organic component incorporation in the sputtered film. Carbon incorporation has already investigated in [41] and believed to be inevitable source of work function determination in ITO. However, defect level of carbon incorporation in MoO_x is required to be investigated and thus work function lowering. One possibility of negative hydrogen ion presence on the sputtered film surface as reported by Dus et al. [44] which in turn react with metal produce metal hydride. Despite it might be not applicable in our case, hydrogen and carbon hybridization on the sputtered film surface and thus work function lowering induced has already showed its potential in field emission display applications [45]. Surface morphology is already reported as possible cause of work function lowering and a correlation between WF and SR was established [46].

In sum, we believe that plasma temperature promoted hydrogen and other reactant in the chamber along with negative electrons and negative ions might accumulate at surface is probable factor to be investigated as part of comprehensive loss analysis study. All of those parameters pose challenge in work function increasing, thus suitable detailed characterization and analysis are required to identify the major factors that impact sputtered film s. Understanding of sputtered film work function's influencing parameters is necessary and pose new driver for the new design rules for technology and process improvement and optimization.

5. Chapter Five: Conclusion and Future Outlook

5. Chapter Five: Conclusion and Future Outlook

5.1 Conclusion

Given the entire theoretical background featured in chapter one and two, MoO_x thin layer for SHJ were deposited with RF sputtering method which is industrial attractive method and robust in tuning material composition properties. Then wafers undergo post deposition annealed process and finally characterized with measurements techniques which are mentioned with detailed specifications in chapter three and chapter four. Accordingly, with sputtering physical conditions optimized starting from available highest power condition, highest argon and oxygen gas available flow and arbitrary oxygen flow, we commenced multiple experiments so that to have trendline about desirable conditions which would give rise to near stoichiometric composition of Molybdenum Oxide. In general, the near stoichiometric version of MoO_x favors lower power conditions at (100W), highest reactive gas flow rate (O₂ flow 100sccm) and mid-range of sputtering ion flow rate (around 100sccm). The accepted near stoichiometric samples were annealed for double time (i.e. for 60min) required for typical contender evaporated MoO_x sample. Although, near desirable chemical atomic ratio of oxygen to molybdenum is achieved, as low as 26 % work function reduction after thermal annealing (from 6.08eV), it is still low in comparison with theoretical work function of MoO₃(6.7eV) However, main explanation is that, work function also dependent on other film physical and /or chemical properties parameters as well as physical conditions samples may undergo and explained in the last section of chapter four. The same samples undergo passivation quality tests and the only enhancement observed due to sputtering damage if samples annealed for 1 hour time and hence yielded cell pseudo efficiency 14.9% at open circuit voltage of 465mV. Flat band voltage measured with C-V technique with nearly 457mV and its relationship to Voc were discussed in the last section of chapter four. Finally, TEM images showed very two thin mixed interfacial layers at between a-Si:H(i) and MoO_x layers and MoO_x and ITO layers which is speculated as the cause for low Voc.

5.2 Future Outlook

Obviously, the master thesis represents a promising foot step into future research work which is immensely required to enhance results with more investigation. Low work function results deserve more optimization on finding suitable a deposition condition for achieving high work function and hence high band bending. Low work function also deserves finding out the right anneal condition to avoid work function degradation to retain strong band bending. The

demand on more specialized investigation of TEM measurements is needed to evaluate the influence of interfacial mixed layers on MoO_x work function, flat band voltage, and hence, solar cell performance.

IV. References and Bibliography

References and Bibliography

1. Paris Climate Change agreement, December 2015., <https://unfccc.int/process-and-meetings/the-paris-agreement/the-paris->,
2. Photovoltaic report, Fraunhofer Institute for Solar Energy Systems, ISE with support of PSE Conferences and Consulting GmbH, August 2018, <https://www.ise.fraunhofer.de/content/dam/ise/de/documents/publications/studies/Photovoltaics-Report.pdf>
3. Martin Bivour, Silicon Heterojunction Solar Cells: Analysis And Basic Understanding, [2015], Fraunhofer Institute for Solar Energy Systems ISE.
4. Denis Pascual Sánchez, Joaquim Puigdollers and Juan M. López, Crystalline silicon Heterojunction solar cells, [2015]. Treball Final del Grau en Enginyeria Física, Universitat Politècnica de Catalunya Barcelona .
5. Kyocera, Principle of Solar Cell-Science behind cell, 2018, https://global.kyocera.com/prdct/solar/spirit/about_solar/cell.html.
6. Thorsten Dullweber et al., Industrial Silicon Solar Cells Applying the Passivated Emitter and Rear Cell (PERC) Concept—A Review, SEPTEMBER 2016, IEEE JOURNAL OF PHOTOVOLTAICS, VOL. 6, NO. 5.
7. REC Solar Pte. Ltd. , Maximizing cell performance, How REC's use of Passivated Emitter Rear Cell technology improves the capture of light and optimizes cell performance, <http://www.recgroup.com>.
8. M. Boccard et al, Silicon-based heterojunction solar cells, EFPL-PV-Lab, [2018], https://pvlab.epfl.ch/heterojunction_solar_cells.
9. Raghu V.K Chavaliet al, [2017], Device physics underlying silicon heterojunction and passivating-contact solar cells: A topical review, Wiley Photovoltaic, DOI: 10.1002/pip.2959.

10. Jimmy Melskens et. al. Passivating Contacts for Crystalline Silicon Solar Cells: From Concepts and Materials to Prospects. IEEE Journal of Photovoltaics, vol. 8, no. 2, [2018], DOI: 10.1109/JPHOTOV.2018.2797106.
11. Luis G. Gerling et. al. Transition metal oxides as hole-selective contacts in silicon heterojunctions solar cells. Solar Energy Materials and Solar Cells [2015] DOI: 10.1016/j.solmat.2015.08.028.
12. Myeong Sook Oh et. al. Improvement of electrical and optical properties of molybdenum oxide thin films by ultralow pressure sputtering method. Journal of Vacuum Science and Technology A 30, 031501 [2012]; DOI: 10.1116/1.3692753.
13. Mark T. Greiner et, al. Transition Metal Oxide Work Functions: The Influence of Cation Oxidation State and Oxygen Vacancies, Advanced Functional Material. [2012], DOI: 10.1002/adfm.201200615.
14. Jonas Geissbühler et. al., 22.5% efficient silicon heterojunction solar cell with molybdenum oxide hole collector. Applied Physics Letters 107, 081601 [2015]; DOI: 10.1063/1.4928747.
15. S. Berg, T. Nyberg. Fundamental understanding and modeling of reactive sputtering process. The Angstrom Laboratory, Uppsala University, Box 534, 75121 Uppsala, Sweden, Thin Solid Films 476 [2005] 215-230.
16. Julia M. Pachlhofer et.al . Industrial-scale sputter deposition of molybdenum oxide thin films: Microstructure evolution and properties. Journal of Vacuum Science and Technology A 35, 021504 [2017]; DOI: 10.1116/1.4973214.
17. Lisa Neusel et al., Selectivity issues of MoO_x based hole contacts, 2017, 7th International Conference on Silicon Photovoltaics, Silicon PV 2017.
18. International Roadmap For Devices And Systems, 2017 Edition Yield Enhancement, The International Roadmap For Devices And Systems, IEEE.

19. Florian [Buchholz](#) , Metal Surface Contamination in c-Si Solar Cell Processing, 2016. [Faculty of Chemistry and Physics of the Technische Universität Bergakademie Freiberg](#).
20. Sander Van Gompel, Standard TXRF on NimbusXP, 2017, IMEC-Leuven.
21. J. Steenbergen, Process specifications: Heat pulse I and II, 2009, IMEC-Leuven.
22. DektakXT Stylus Profiler, User manual, Bruker Nano Surfaces Business, 2011, Tucson, Arizona 85756.US.
23. Michael Sing, Physikalisches Institut and Röntgen Center for Complex Material Systems (RCCM) Universität Würzburg, Germany, <https://www.cond-mat.de/events/correl14/talks/sing.pdf>.
24. Jolm F. Moulder et al., Handbook of X-ray Photoelectron Spectroscopy, 1992, published by Perkin-Elmer Corporation, US.
25. Jožef Visočnik, Analysis of light elements in solids by elastic recoil detection analysis, 2008, University of Ljubljana, 2nd seminar, 4th year of graduate physics studies.
26. Jandel RM3000 Testing unit, Instruction Manual, Jandel Engineering, <http://four-point-probes.com/rm3000-test-unit-with-pc-software/>.
27. Dieter K. Schroder, Semiconductor Material And Device Characterization, third edition, 2006, Arizona State University, Published by John Wiley and Sons, Inc., US.
28. Maarten Debucquoy et al. , Luminescence setup BT Imaging: work regulations , 2016, IMEC-Leuven, Internal procedure (Confidential).
29. S. Bowden et al., Implied- V_{oc} And Suns- V_{oc} Measurements In Multi-crystalline Solar Cells, University Center of Excellence in Photovoltaics, School of Electrical and Computer Engineering, Georgia Institute of Technology, Atlanta, GA 30332–0250 USA
30. SINTON Suns-Voc-Post-Diffusion-Process-Control WCT-120, SINTON Product note, 2011, www.sintoninstruments.com

31. Keithley, Capacitors Using the Model 4200-SCSPParameter Analyzer manual, www.Keithley.com
32. Miron J. Cristea, Capacitance-voltage profiling techniques for characterization of semiconductor materials and devices, 'Politehnica' University of Bucharest, 313 Spl. Independentei, Bucharest, Romania; E-mail: miron.cristea@gmail.com.
33. MyScope training for advanced research, Transmission Electron Microscope, Training module, Australian Microscopy and Microanalysis research Center, www.ammrf.org.au/myscope/tem/introduction.
34. Pavel Zinin, Transmission Electron Microscope, Lecture 14, HIGP, University of Hawaii, Honolulu, USA.
34. Dominik J. Green et al., Transmission Electron Microscopy And Computer-Aided Image Processing For 3D Structural Analysis Of Macromolecules, University of California Davis. U.S <https://koppa.jyu.fi/en/courses/164631/course-literature/transmission-electron-microscopy>
35. Romyana V. Petrova, Quantitative High-Angle Annular Dark Field Scanning Transmission Electron Microscopy For Materials Science, dissertation for University of Central Florida, U.S, http://etd.fcla.edu/CF/CFE0001267/Petrova_Romyana_V_200608_PhD.pdf.
36. Dr. Rudy Schlaf, Calibration of Photoemission Spectra and Work Function Determination, <http://rsl.eng.usf.edu/Documents/Tutorials/PEScalibration.pdf>.
37. IMEC-Leuven -<https://www.imec-int.com/en/home>.
38. Naveen K. Elumalai et al., Open circuit voltage of organic solar cells: an in-depth review, 2015, DOI: 10.1039/c5ee02871j, the royal society of chemistry journal .
39. Miroslav Mikolášek, Silicon Heterojunction Solar Cells: The Key Role of Heterointerfaces and their Impact on the Performance, Chapter 4, <http://dx.doi.org/10.5772/65020>, INTECH
40. Martin Bivour et al., Principles Of Carrier-Selective Contacts Based On Induced Junctions, 2017, 33rd European PV Solar Energy Conference and Exhibition.

41. Kiyoshi Sugiyama, Dependence of indium–tin–oxide work function on surface cleaning method as studied by ultraviolet and x-ray photoemission spectroscopies, 1999, : <https://doi.org/10.1063/1.371859>, Journal Of Applied Physics.
42. Xiaoyang Pan, Defective TiO₂ with oxygen vacancies: synthesis, properties and photocatalytic applications, 2013, DOI: 10.1039/c3nr00476g, the royal society of chemistry.
43. Chang S. Kang, Characterization of resistivity and work function of sputtered-TaN film.
44. R. Duś et al., The Response of Work Function of Thin Metal Films to Interaction with Hydrogen, Proceedings of the Professor Stefan Mróz Symposium, Institute of Physical Chemistry, Polish Academy of Sciences Kasprzaka 44/52, 01-224 Warszawa, Poland. corresponding author; e-mail: dus@ichf.edu.pl.
45. Sk. F. Ahmed et al., Silicon incorporated Diamond like Carbon films for field emission display, 2014, Thin Film & Nanoscience Laboratory, Department of Physics, Nanoscience and Technology center Jadavpur University, India. Email; kalyan_chattopadhyay@yahoo.com.
46. W. Li, On the correlation between surface roughness and work function in copper, 2005, <http://dx.doi.org/10.1063/1.1849135>, The Journal Of Chemical Physics.